A Rigid-Field Hydrodynamics approach to modelling the magnetospheres of massive stars

R. H. D. Townsend,[*] S. P. Owocki and A. ud-Doula
Bartol Research Institute, Department of Physics & Astronomy, University of Delaware, Newark, DE 19716, USA

ABSTRACT

We introduce a new Rigid-Field Hydrodynamics approach to modelling the magnetospheres of massive stars in the limit of very strong magnetic fields. Treating the field lines as effectively rigid, we develop hydrodynamical equations describing the one-dimensional flow along each, subject to pressure, radiative, gravitational and centrifugal forces. We solve these equations numerically for a large ensemble of field lines to build up a three-dimensional time-dependent simulation of a model star with parameters similar to the archetypal Bp star σ Ori E. Since the flow along each field line can be solved independently of other field lines, the computational cost of this approach is a fraction of an equivalent magnetohydrodynamical treatment.

The simulations confirm many of the predictions of previous analytical and numerical studies. Collisions between wind streams from opposing magnetic hemispheres lead to strong shock heating. The post-shock plasma cools initially via X-ray emission, and eventually accumulates into a warped, rigidly rotating disc defined by the locus of minima of the effective (gravitational plus centrifugal) potential. However, a number of novel results also emerge. For field lines extending far from the star, the rapid area divergence enhances the radiative acceleration of the wind, resulting in high shock velocities (up to $\sim$3000 km s^{-1}) and hard X-rays. Moreover, the release of centrifugal potential energy continues to heat the wind plasma after the shocks, up to temperatures around twice those achieved at the shocks themselves. Finally, in some circumstances the cool plasma in the accumulating disc can oscillate about its equilibrium position, possibly due to radiative cooling instabilities in the adjacent post-shock regions.

Key words: hydrodynamics – stars: magnetic fields – stars: mass-loss – stars: rotation – gamma-rays: theory – X-rays: stars.

1 INTRODUCTION

During their main-sequence evolution, massive, hot stars lack the envelope convection zones that generate magnetic fields in the Sun and other cool stars. Nonetheless, since the 1970s it has been known that a small, chemically peculiar subset – the Bp stars – possess global-scale fields at the kilogauss level (e.g. Borra & Landstreet 1979; Borra, Landstreet & Thompson 1983). Moreover, the significant advances in spectropolarimetric instrumentation over the past three decades have led to the discovery of $\sim$100–1000 G fields in a number of other massive stars, including two O-type stars (θ^1 Ori C – Donati et al. 2002; HD 191612 – Donati et al. 2006a), X-ray bright B-type stars (τ Sco – Donati et al. 2006b) and a number of slowly pulsating B-type stars (Hubrig et al. 2007).

On the theoretical side, the genesis of massive-star fields remain the subject of some controversy, with fossil-origin expla-

nations (e.g. Ferrario & Wickramasinghe 2005, 2006) competing against dynamo models involving processes such as core convection (Charbonneau & MacGregor 2001), Tayler–Spruit instabilities (Mullan & MacDonald 2005) and global Rossby modes (Airapetian 2000). However, considerable progress has been made in understanding how the magnetic fields channel and confine the stars' dense, supersonic, radiatively driven winds. The seminal Magnetically Confined Wind Shock (MCWS) model of Babel & Montmerle (1997a,b) conjectured that wind streams from opposing footpoints collide near the summits of closed magnetic loops, shock heating the plasma to temperatures $T \sim 10^6$–10^7 K at which thermal X-ray emission becomes important. Subsequent magnetohydrodynamical (MHD) simulations by ud-Doula & Owocki (2002) confirmed the basic MCWS paradigm, and led to the development of a quantitative magnetic wind-shock model for the hard X-ray emission of θ^1 Ori C, which shows good agreement with *Chandra* observations of the star (Gagné et al. 2005).

MHD simulation is a powerful tool for modelling magnetic wind confinement, but becomes increasingly difficult toward large values

[*]E-mail: rhdt@bartol.udel.edu

of the confinement parameter η, defined as the ratio between magnetic and kinetic energy densities (ud-Doula & Owocki 2002). At large η, the field lines are scarcely affected by the plasma flowing along them. Such a rigid character implies a high Alfvén speed, and in turn a short numerical time-step in MHD codes to ensure Courant stability (Press et al. 1992). In the case of the Bp stars – characterized by confinement parameters up to $\eta \sim 10^7$ – the required time-steps are in fact too short for MHD simulation to be practical.

For these strongly magnetic stars, Townsend & Owocki (2005, hereafter TO05) expanded on previous work by Michel & Sturrock (1974) and Nakajima (1985) to develop a Rigidly Rotating Magnetosphere (RRM) model based on the simplifying ansatz that field lines are completely rigid. The RRM model does not consider the detailed physics of the wind streams feeding into the collision shocks, but instead focuses on the fate of the post-shock plasma after it has radiatively cooled back down to photospheric temperatures. In a rotating star, this plasma has a tendency to settle into magnetohydrostatic stratifications centred on local minima of the effective (gravitational plus centrifugal) potential. For an oblique dipole magnetic field, the locus of these potential wells resembles a warped disc that corotates rigidly with the star. When applied to the archetypal magnetic Bp star σ Ori E (HD 37479; B2Vpe), the Hα emission from the disc plasma shows very good agreement with that seen in observations (Townsend, Owocki & Groote 2005), lending strong support to the model.

Building on the success of the RRM model, this paper presents a new Rigid-Field Hydrodynamics (RFHD) approach to modelling massive-star magnetospheres in the strong-field limit. We again assume that the field lines behave as completely rigid, but we now explicitly consider the time-dependent evolution of the magnetically channelled wind. This approach not only furnishes a dynamical picture of disc accumulation, it also opens up the possibility of synthesizing observables for the shock-heated wind plasma, across a broad range of wavelengths extending from X-ray through to radio.

In the following section, we consider the one-dimensional (1D) hydrodynamical problem of flow along each rigid field line, with an emphasis on the specific, simple case of a dipole field topology. In Section 3, we introduce a numerical code that solves the governing equations along many field lines to build up a three-dimensional (3D) simulation of a massive-star magnetosphere. We use this code in Section 4 to model a star loosely based on σ Ori E; results from these simulations are presented and analysed in Section 5. In Section 6, we examine some of the broader issues pertaining to the RFHD approach, and in Section 7, we summarize the paper.

2 RIGID-FIELD HYDRODYNAMICS

As we discuss above, the key notion of the RFHD approach is that the magnetic field at sufficiently high strengths behaves as if it were rigid. This rigid field is anchored to the star, and corotates with it. Under the frozen flux condition of ideal MHD, plasma is constrained to flow along field lines, and it therefore describes trajectories that are fixed in the corotating frame.

The shape of these trajectories is specified a priori by the chosen magnetic topology. However, the plasma state (density, temperature, velocity etc.) along each field line is determined by the 1D hydrodynamical problem of flow along a tube with changing cross-sectional area. Here, the 'tube' can be identified explicitly with a magnetic flux tube, whose area varies inversely with the local magnetic flux density $B \equiv |\boldsymbol{B}|$ in order to ensure that $\nabla \cdot \boldsymbol{B} = 0$. The character

of the flow is dictated primarily by the forces that act to accelerate or decelerate the plasma: pressure gradients, gravity, the centrifugal force and radiative forces. Perhaps surprisingly, magnetic and Coriolis forces play no direct role in the 1D flow problem, because they are always directed perpendicular to the instantaneous velocity vector $\boldsymbol{v}$. (This vector is itself everywhere parallel to the field-line tangent vector $\boldsymbol{e}_s \equiv \boldsymbol{B}/B$.) In fact, these forces act similarly to the centripetal force of a circular orbit, furnishing a net acceleration perpendicular to $\mathbf{v}$ that leads to curved plasma trajectories yet does no work.

2.1 Euler equations

To elaborate on the foregoing discussion, we introduce the Euler equations in conservation form for the 1D hydrodynamical problem composing RFHD:

$$\frac{\partial \rho}{\partial t} + \frac{1}{A}\frac{\partial}{\partial s}(A\rho v) = 0, \tag{1}$$

$$\frac{\partial \rho v}{\partial t} + \frac{1}{A}\frac{\partial}{\partial s}(A\rho v^2) + \frac{\partial p}{\partial s} = \rho(\boldsymbol{g}_{\text{eff}} + \boldsymbol{g}_{\text{rad}}) \cdot \boldsymbol{e}_s, \tag{2}$$

$$\frac{\partial \rho e}{\partial t} + \frac{1}{A}\frac{\partial}{\partial s}[Av(\rho e + p)] = \rho v(\boldsymbol{g}_{\text{eff}} + \boldsymbol{g}_{\text{rad}}) \cdot \boldsymbol{e}_s + \Lambda. \tag{3}$$

Here, the independent variables are the arc distance s along the field line (relative to some arbitrary zero-point) and time t, while the dependent variables are density ρ, pressure p, velocity $v \equiv |\boldsymbol{v}|$ and total energy per unit mass e. The term $A(s)$ describes the spatially varying cross-sectional area of the flow tube, and depends on the magnetic topology; expressions for this term in the case of a dipole field are derived in the following section. The acceleration vectors $\boldsymbol{g}_{\text{eff}}$ and $\boldsymbol{g}_{\text{rad}}$ are due to the effective gravity and the radiative line force, respectively, and are considered in greater detail in Sections 2.3 and 2.5. Interrelationships between ρ, p, v and e are determined from equations of state and total energy, defined in Section 2.6. Finally, the term Λ is the volumetric energy loss rate due to cooling processes, and is discussed in Section 2.7. For reasons elaborated there, we do not include the effects of thermal conduction in the energy conservation equation (3).

By setting all velocities and time derivatives to zero, the momentum conservation equation (2) reduces to the condition of magnetohydrostatic equilibrium, in which body forces are balanced by pressure gradients. Because it furnishes the basis of the precursor RRM model, we review this static limit in Appendix A.

2.2 Dipole field geometry

Although the RFHD approach is in principle applicable to arbitrary magnetic topologies, the present study focuses on the simple case of an oblique dipole field. Let (r, θ, ϕ) be the spherical polar coordinates in the reference frame aligned with the rotation axis; likewise, let $(\tilde{r}, \tilde{\theta}, \tilde{\phi})$ be the corresponding coordinates in the frame aligned with the dipole magnetic axis. (This is the same notation as adopted in TO05.) As illustrated in Fig. 1, the magnetic axis is tilted with respect to the rotation axis by the magnetic obliquity β.

In the magnetic reference frame, the magnetic flux vector is expressed as

$$\boldsymbol{B} = \frac{B_0}{2(\tilde{r}/R_{\text{p}})^3}\left(2\cos\tilde{\theta}\,\boldsymbol{e}_{\tilde{r}} + \sin\tilde{\theta}\,\boldsymbol{e}_{\tilde{\theta}}\right), \tag{4}$$
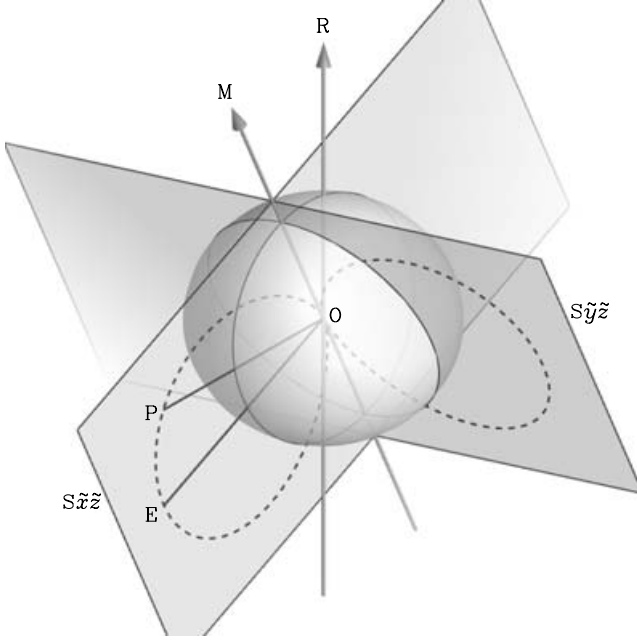
Figure 1. An illustration of the oblique dipole geometry described in the text. The star is shown as an oblate spheroid centred on the origin O, with magnetic axis M and rotational axis R; the angle MOR is the obliquity β. The surfaces S$\tilde{x}\tilde{z}$ and S$\tilde{y}\tilde{z}$ are the $\tilde{x}$–$\tilde{z}$ and $\tilde{y}$–$\tilde{z}$ planes of the magnetic reference frame, corresponding to azimuths $\tilde{\phi} = (0°, 180°)$ and $(90°, 270°)$, respectively. Two selected field lines, having $\tilde{\phi} = 0°$ and $90°$, are shown by dotted lines; on the $\tilde{\phi} = 0°$ field line, E labels the magnetic equator, and P a point on the field line. The line OE (measured by convention in units of the rotational polar radius R_p) gives the magnetic shell parameter L; likewise, EP defines the arc distance coordinate s of the point P. (In this case, $s < 0$, because P lies in the northern magnetic hemisphere.) OP is the radial coordinate $\tilde{r} = r$ of P, and the angle MOP (ROP) gives the corresponding colatitude $\tilde{\theta}$ (θ) in the magnetic (rotational) reference frame.

where B_0 sets the overall field strength,[1] R_p is the rotational polar radius (a convenient normalizing length) and $e_{\tilde{r}}$ and $e_{\tilde{\theta}}$ are the unit basis vectors in the magnetic radial and polar directions, respectively. From this expression, the tangent vector e_s is obtained as

$$e_s = \frac{\boldsymbol{B}}{B} = \frac{1}{\sqrt{1 + 3\cos^2\tilde{\theta}}} \left(2\cos\tilde{\theta}\, e_{\tilde{r}} + \sin\tilde{\theta}\, e_{\tilde{\theta}} \right). \tag{5}$$

This result also follows from the parametric equation for a dipole field line:

$$\frac{\tilde{r}}{R_p} = L\sin^2\tilde{\theta} \tag{6}$$

(e.g. Nakajima 1985; Babel & Montmerle 1997a), where the magnetic shell parameter L measures the maximal radius reached by the field line, in units of R_p. To label a field line uniquely, it suffices to specify L and the magnetic azimuthal coordinate $\tilde{\phi}$ defining the half-plane that contains the line.

The spatial variable s in the 1D hydrodynamical equations (1)–(3) is the arc distance along each field line, and is found from the dipole line element

$$ds^2 = d\tilde{r}^2 + \tilde{r}^2\, d\tilde{\theta}^2 = L^2 R_p^2 \sin^2\tilde{\theta} \left(1 + 3\cos^2\tilde{\theta} \right) d\tilde{\theta}^2. \tag{7}$$

[1] For an aligned dipole ($\beta = 0$), B_0 corresponds to the polar field strength; however, this does not generally hold when $\beta > 0$ due to the oblateness of the star (Section 2.4).

Solving this differential equation for s, we obtain

$$\frac{s}{R_p} = -\frac{L}{2}\left[\frac{\sinh^{-1}(\sqrt{3}\cos\tilde{\theta})}{\sqrt{3}} + \cos\tilde{\theta}\sqrt{1 + 3\cos^2\tilde{\theta}} \right], \tag{8}$$

where the constant of integration is chosen to place the origin $s = 0$ at the magnetic equator, $\tilde{\theta} = 90°$. The negative sign on the right-hand side arises from selecting the positive root of equation (7), so that s increases in the same direction as $\tilde{\theta}$, and s is negative (positive) in the northern (southern) magnetic hemisphere. Since this equation is transcendental, calculation of the inverse function $\tilde{\theta}(s)$ must be undertaken numerically (Section 3.2).

The footpoints of the field line in the northern and southern magnetic hemispheres are denoted as s_N and s_S, respectively. For a spherical star with radius R_*,

$$\frac{s_N}{R_*} = -\frac{s_S}{R_*} = -\frac{L}{2}\left[\frac{\sinh^{-1}\sqrt{3 - 3/L}}{\sqrt{3}} \right. $$
$$\left. + \sqrt{1 - 1/L}\sqrt{4 - 3/L} \right]. \tag{9}$$

However, for an oblate star (cf. Section 2.4) calculation of s_N and s_S once again must proceed numerically (Section 3.2).

The variation in the cross-sectional area of each flow tube is determined by the requirement of magnetic flux conservation. If A_{eq} is the area at the magnetic equator, then the area A at any colatitude $\tilde{\theta}$ must satisfy

$$A B = A_{eq} B_{eq}, \tag{10}$$

where

$$B_{eq} = \frac{B_0}{2L^3} \tag{11}$$

is the field strength at the magnetic equator. Eliminating B with the help of equations (4) and (6), we find that

$$\frac{A}{A_{eq}} = \frac{\sin^6\tilde{\theta}}{\sqrt{1 + 3\cos^2\tilde{\theta}}}. \tag{12}$$

Combined with the inverse function $\tilde{\theta}(s)$, this expression is used to construct the area function $A(s)$ appearing in the Euler equations (1)–(3).

In addition to the area function A, finite-volume hydrodynamical codes such as VH-1 (cf. Section 3) require specification of the volume function

$$V \equiv \int A\,ds. \tag{13}$$

To obtain V in the present case, we note from equations (7) and (12) that

$$A\,ds = A\frac{ds}{d\tilde{\theta}}\,d\tilde{\theta} = L A_{eq} R_p \sin^7\tilde{\theta}\,d\tilde{\theta}. \tag{14}$$

It therefore follows that

$$\frac{V}{A_{eq} R_p} = L\left[-\frac{7}{320}(25\cos\tilde{\theta} - 5\cos 3\tilde{\theta} + \cos 5\tilde{\theta}) \right.$$
$$\left. + \frac{1}{448}\cos 7\tilde{\theta} \right], \tag{15}$$

and, as with $A(s)$, the inverse function $\tilde{\theta}(s)$ is used to find $V(s)$.

2.3 Effective potential

The effective gravitational acceleration $\boldsymbol{g}_{eff}$ in equations (2) and (3) combines the Newtonian gravity with the centrifugal force associated with enforced corotation. Together, these forces are derived

from a scalar effective potential Φ_{eff}:

$$\boldsymbol{g}_{\mathrm{eff}} = -\nabla\Phi_{\mathrm{eff}}. \tag{16}$$

Within the Roche (point-mass) approximation, this effective potential is given by

$$\Phi_{\mathrm{eff}} = -\frac{GM_*}{r} - \frac{1}{2}\Omega^2\varpi^2. \tag{17}$$

Here, M_* is the stellar mass, Ω the angular rotation frequency and $\varpi \equiv r\sin\theta$ is the distance from the rotation axis. Combining the above two expressions, the effective gravity term in the momentum and energy conservation equations (2) and (3) is found as

$$\boldsymbol{g}_{\mathrm{eff}} \cdot \boldsymbol{e}_s = -\frac{GM_*}{r^2}\boldsymbol{e}_r \cdot \boldsymbol{e}_s + \Omega^2\varpi\,\boldsymbol{e}_\varpi \cdot \boldsymbol{e}_s, \tag{18}$$

where $\boldsymbol{e}_r$ and $\boldsymbol{e}_\varpi$ are the unit vectors in the r and ϖ directions, respectively. For a dipole field (Section 2.2),

$$\boldsymbol{e}_r \cdot \boldsymbol{e}_s = \boldsymbol{e}_{\tilde{r}} \cdot \boldsymbol{e}_s = \frac{2\cos\tilde{\theta}}{\sqrt{1 + 3\cos^2\tilde{\theta}}} \equiv \cos\chi \tag{19}$$

gives the component of the local radial vector projected along the field line. The angle χ introduced in this expression, being that between the field line and the radial vector, also appears below in the equations governing the radiative acceleration.

2.4 Stellar properties

In addition to generating the effective gravity, Φ_{eff} determines the shape and surface properties of the oblate, centrifugally distorted star. In the Roche approximation (equation 17), the surface is an equipotential whose radius r_* varies with rotational colatitude θ as

$$\frac{r_*}{R_{\mathrm{p}}} = \frac{3}{w\sin\theta}\cos\left[\frac{\pi + \cos^{-1}(w\sin\theta)}{3}\right] \tag{20}$$

(e.g. Cranmer 1996). Here,

$$w \equiv \Omega\sqrt{\frac{27R_{\mathrm{p}}^3}{8GM_*}} \tag{21}$$

is the normalized rotation angular frequency, with $w = 1$ corresponding to critical rotation.

Because of gravity darkening (von Zeipel 1924), the flux emitted by a rotating, radiative stellar envelope varies in proportion to the local effective gravity $|\boldsymbol{g}_{\mathrm{eff}}|$. However, in evaluating the radiative acceleration (Section 2.5) and the rate of inverse Compton cooling (Section 2.6), we choose for simplicity to treat the circumstellar radiation field as originating from a spherically symmetric point source of luminosity L_*. For consistency, we therefore neglect the variation of the surface flux, setting it to the constant value

$$F_* \equiv \frac{L_*}{\Sigma_0}. \tag{22}$$

Here, Σ_0 is the total surface area of the oblate star, which can be approximated to within 2 per cent by the polynomial:

$$\Sigma_0 = 4\pi R_{\mathrm{p}}^2(1 + 0.19444w^2 + 0.28053w^4 - 1.9014w^6$$
$$+ 6.8298w^8 - 9.5002w^{10} + 4.6631w^{12}) \tag{23}$$

(Cranmer 1996). From F_* and the Stefan–Boltzmann law, a nominal stellar surface temperature is defined as

$$T_* = \left(\frac{F_*}{\sigma}\right)^{1/4}. \tag{24}$$

2.5 Radiative acceleration

To obtain an expression for the radiative acceleration $\boldsymbol{g}_{\mathrm{rad}}$ we employ the Castor, Abbott & Klein (1975, hereafter CAK) formalism for line-driven stellar winds. For simplicity, the star is treated as a point source of radiation, giving an acceleration

$$\boldsymbol{g}_{\mathrm{rad}} = \frac{1}{1-\alpha}\frac{\kappa_{\mathrm{e}}L_*\bar{Q}}{4\pi r^2 c}\left(\frac{|\delta_v|}{\rho c\bar{Q}\kappa_{\mathrm{e}}}\right)^\alpha \boldsymbol{e}_r \tag{25}$$

(e.g. Owocki 2004). Here, α is the CAK power-law index, $\bar{Q}$ is the dimensionless line strength parameter introduced by Gayley (1995), L_* is the stellar luminosity (Section 2.4) and κ_{e} is the electron-scattering opacity, $\approx 0.34\,\mathrm{cm}^2\,\mathrm{g}^{-1}$ for a fully ionized solar-composition plasma. The term δ_v, a measure of the local velocity gradient that determines the Sobolev (1960) optical depth, is defined as

$$\delta_v \equiv \boldsymbol{e}_r \cdot \nabla(\boldsymbol{e}_r \cdot \boldsymbol{v}). \tag{26}$$

From equation (19),

$$\boldsymbol{e}_r \cdot \boldsymbol{v} = v\cos\chi, \tag{27}$$

and thus

$$\delta_v = \boldsymbol{e}_r \cdot \nabla(v\cos\chi) = \cos\chi\,\boldsymbol{e}_r \cdot \nabla v. \tag{28}$$

(The second equality follows because χ is a function of $\tilde{\theta}$ alone, and therefore commutes with the radial directional derivative $\boldsymbol{e}_r \cdot \nabla$.) Expanding out the gradient operator in the magnetic reference frame, we obtain

$$\delta_v = \cos\chi\left(\frac{\partial v}{\partial\tilde{r}}\right)_{\tilde{\theta}}. \tag{29}$$

To evaluate the radial derivative in this latter equation, it is necessary to know the flow velocity on field lines adjacent to the one under consideration. In order to avoid this complication, we make the simplifying assumption that the polar velocity derivate vanishes,

$$\left(\frac{\partial v}{\partial\tilde{\theta}}\right)_{\tilde{r}} \approx 0. \tag{30}$$

As we demonstrate in Appendix B, this assumption implies that

$$\left(\frac{\partial v}{\partial\tilde{r}}\right)_{\tilde{\theta}} = \left(\frac{\partial v}{\partial s}\right)_L \sec\chi. \tag{31}$$

Substituting this expression back into equation (29) yields

$$\delta_v = \left(\frac{\partial v}{\partial s}\right)_L, \tag{32}$$

which in combination with equation (25) leads to the final expression for the radiative acceleration,

$$\boldsymbol{g}_{\mathrm{rad}} = \frac{1}{1-\alpha}\frac{\kappa_{\mathrm{e}}L_*\bar{Q}}{4\pi r^2 c}\left(\frac{|\partial v/\partial s|}{\rho c\bar{Q}\kappa_{\mathrm{e}}}\right)^\alpha \boldsymbol{e}_r. \tag{33}$$

To conform with our earlier notation (cf. Section 2.1), here we have dropped the 'L' subscript on the velocity gradient $\partial v/\partial s$.

The central approximation here, equation (30), is equivalent to assuming that v – which might more correctly be termed the flow speed – depends only on $\tilde{r}$, although of course the local flow direction still depends on $\tilde{\theta}$ since it follows the field-line orientation. Analysis based on 2D MHD simulations (cf. Owocki & ud-Doula 2004) indicates that this approximation is well justified in the regions of rapid wind acceleration near to the star. Moreover, in the present work we have carried out a posteriori checks using an ensemble of neighbouring 1D RFHD calculations, and find that

the error in $\boldsymbol{g}_{\mathrm{rad}}$ arising from using equation (32) for δ_v instead of the exact expression (29) is typically 10 per cent or less throughout the radiatively driven regions of the magnetosphere.

We emphasize that the benefit from this approximation is significant. Because equation (33) depends only on the velocity gradient along a field line, it allows the flow to be modelled completely independently of other field lines. Not only is this advantageous in terms of computational efficiency, it also simplifies the interpretation and analysis of simulation results (Section 5).

2.6 Equations of state and energy

We assume an ideal gas, so that

$$p = \frac{\rho kT}{\mu u}, \tag{34}$$

with T the temperature and u the atomic mass unit. The mean molecular weight μ is determined from an expression appropriate to a fully ionized mixture:

$$\mu = \left[2X + \frac{3}{4}(1 - X - Z) + \frac{Z}{2} \right]^{-1}, \tag{35}$$

where X and Z are the usual hydrogen and metal mass fractions. The accompanying equation for the specific (per-unit-mass) total energy is

$$e = \frac{1}{\gamma - 1} \frac{kT}{\mu u} + \frac{v^2}{2}, \tag{36}$$

where γ is the ratio of specific heats.

2.7 Cooling and thermal conduction

The volumetric cooling rate Λ in the energy conservation equation (3) is evaluated as the sum of two terms,

$$\Lambda = \Lambda_{\mathrm{at}} + \Lambda_{\mathrm{ic}}, \tag{37}$$

representing contributions from atomic processes and inverse Compton scattering by thermal electrons, respectively. The first term is calculated from

$$\Lambda_{\mathrm{at}} = n_e n_p \mathcal{L}(T), \tag{38}$$

where

$$n_p = \frac{X}{u} \rho \tag{39}$$

and

$$n_e = \frac{1 + X}{2u} \rho \tag{40}$$

define the proton and electron number densities, respectively. The temperature-dependent cooling coefficient $\mathcal{L}$ is obtained from the curve published by MacDonald & Bailey (1981).

The inverse Compton term Λ_{ic} is evaluated with the aid of equation (4) of White & Chen (1995),

$$\Lambda_{\mathrm{ic}} = 4 \frac{\kappa_e}{c} n_e U_{\mathrm{ph}} kT. \tag{41}$$

(Note that in their equation 5, these authors define the symbol Λ_{ic} differently than above.) Here,

$$U_{\mathrm{ph}} = \frac{L_*}{4\pi r^2 c} \tag{42}$$

is the energy density associated with the star's radiation field, evaluated in the same point-star limit as the radiative acceleration (Section 2.5).

We have elected to neglect the effects of thermal conduction in the energy conservation equation, because to include these properly requires addressing a large number of issues that are beyond the present scope. These centre on uncertainties both in the treatment of departures from the classical Spitzer (1962) thermal conductivity (e.g. Levinson & Eichler 1992; Pistinner & Eichler 1998), and in the incorporation of heat flux saturation near shocks and other regions of steep temperature gradients (see Lacey 1988; Bandiera & Chen 1994, and references therein). Moreover, apart from these physical difficulties, proper inclusion of conduction in a hydrodynamical code is a challenging task, particularly in the context of accurately modelling the kind of strong shocks that occur in our simulations (see e.g. Reale 1995). We thus defer consideration of thermal conduction to future work.

3 THE RFHD CODE

As discussed in Section 2.5, the utility of the approximate expression (32) for the velocity gradient term δ_v lies in the fact that the flow along each individual field line may be simulated completely independently of other field lines. Thus, by performing many separate 1D simulations for differing field lines and piecing them together, a 3D hydrodynamical metasimulation of a massive-star magnetosphere can be built up at a fraction of the computational cost of an equivalent MHD calculation.

Each individual 1D simulation requires solution of the Euler equations (1)–(3), and for this we employ a customized version of the VH-1 hydrodynamical code developed by J. Blondin and colleagues. VH-1 is a finite volume code based on the Lagrangian version of the piecewise parabolic method (PPM) devised by Colella & Woodward (1984). The modifications to VH-1 primarily encompass incorporation of the dipole geometry (Section 2.2), acceleration terms (Sections 2.3 and 2.5) and cooling (Section 2.7) specific to the RFHD problem. We do not discuss these modifications in detail, but in the following sections we highlight specific issues that arose during the code development phase.

3.1 Grid design

The Eulerian grid in VH-1 must be designed with care, to ensure that regions of physical interest are properly resolved, and to avoid the generation of spurious numerical instabilities. To this end, we divide the grid into three domains. The two 'surface' domains are each composed of a fixed number N_s of zones, extending from the surface footpoints $s = s_N, s_S$ (cf. Section 3.2) to somewhat above the expected position of the sonic point $|v| = a_*$. (Here $a_* \equiv \sqrt{kT_*/\mu u}$ denotes the isothermal sound speed at the surface, with T_* the stellar surface temperature introduced in Section 2.4.) These zones are non-uniform, with the size of each zone being 1.1 times that of its neighbour closer to the stellar surface. With their high spatial resolution, the surface domains are designed to resolve the smooth transition of the wind from a subsonic, near-hydrostatic state to a supersonic outflow.

The third, 'magnetosphere' domain spans the physically interesting regions of the circumstellar environment, and is composed of N_m zones of uniform size $ds \approx (s_S - s_N)/N_s$, that bridge between the two thin surface domains. In determining an appropriate value for N_m, we are motivated by a desire to resolve the dense, corotating disc predicted by the RRM model to accumulate at local minima of the effective potential (see TO05; see also Appendix A). As demonstrated in the appendix, the scaleheight of this disc is independent of the magnetic shell parameter L when L becomes large. Thus, we

vary N_m with L according to the simple formula

$$N_m = \text{int}(\Delta_d L + \Delta_* L^{-1/2}), \tag{43}$$

where int() denotes the integer part. The first term in the parentheses ensures that the disc remains properly resolved at large L, with a constant number of zones per asymptotic scaleheight h_∞ (cf. equation A9); while the second is an ad hoc addition that increases the spatial resolution near the star. The parameters Δ_d and Δ_* are adjusted to achieve the desired spatial resolution in the far- and near-star limits.

3.2 Field-line coordinates

To determine the arc distance coordinates (s_N, s_S) of the field-line footpoints, required in setting up the Eulerian grid (Section 3.1), we solve the equation

$$r_* = L R_p \sin^2 \tilde{\theta} \tag{44}$$

to find the magnetic colatitudes ($\tilde{\theta}_N$, $\tilde{\theta}_S$) associated with each footpoint. (The footpoints are not mirror symmetric about the magnetic equator unless $w = 0$ or $\beta = 0°$.) The corresponding values of s then follow from equation (8). In the above equation, r_* is a function of the rotational colatitude θ (cf. equation 20); thus, it depends implicitly on $\tilde{\theta}$ and $\tilde{\phi}$ via the coordinate transformation between magnetic and rotational reference frames (see Fig. 1). To solve this equation, we use Brent's algorithm (Press et al. 1992).

Once the Eulerian grid is established, we calculate $\tilde{\theta}$ at each zone boundary from the corresponding s values, by inverting equation (8). For this, we use a Newton–Raphson iteration operating on $\cos \tilde{\theta}$, starting from the initial guess

$$\cos \tilde{\theta} = -s \left[L R_p \left(\frac{\sinh^{-1} \sqrt{3}}{2\sqrt{3}} + 1 \right) \right]^{-1}. \tag{45}$$

After each Lagrangian step of the PPM algorithm, the advection of zone boundaries means that the $\tilde{\theta}$ values must be updated. The Newton–Raphson iteration is in this case too slow to be useful, so we instead evaluate $\tilde{\theta}$ by cubic-spline interpolation (Press et al. 1992) from the stored Eulerian-grid values.

3.3 Initial state

The initial, $t = 0$, state for simulations is based on an spherically symmetric, accelerating wind. The velocity is obtained by projecting a canonical velocity law on to field lines:

$$v = v_\infty \left[1 - \frac{r_*}{r} \right]^{1/2} \cos \chi. \tag{46}$$

Here, v_∞ is the terminal velocity obtained from a non-rotating, point-star CAK model:

$$v_\infty = \sqrt{\frac{\alpha}{1 - \alpha} \frac{2 G M_*}{R_p}}. \tag{47}$$

The density is likewise obtained from the condition of steady spherical outflow:

$$\rho = \frac{\dot{M}}{4\pi r^2 v}, \tag{48}$$

where now

$$\dot{M} = \frac{L_*}{c^2} \frac{\alpha}{\alpha - 1} \left[\frac{\bar{Q} \Gamma_e}{1 - \Gamma_e} \right]^{(1-\alpha)/\alpha} \tag{49}$$

is the CAK mass-loss rate, with

$$\Gamma_e \equiv \frac{\kappa_e L_*}{4\pi G M_* c}, \tag{50}$$

the Eddington parameter associated with electron scattering. By assuming an isothermal initial flow, with $T = T_*$, the pressure p is obtained from the equation of state (34).

3.4 Boundary conditions

Boundary conditions are implemented in VH-1 by setting dependent variables (ρ, p, v, e) in ghost zones at both ends of the grid. To allow for the possibility of outflow and inflow, we fix only the density and pressure in the ghost zones, as $\rho = \rho_*$ and $p = p_*$. The stellar density ρ_* can be chosen with some degree of latitude, so long as it remains appreciably above the wind density

$$\rho_s = \frac{\dot{M}}{4\pi r_*^2 a_*} \tag{51}$$

at the sonic point; we find that a choice $\rho_* = 10 \rho_s$ gives a smooth and steady wind outflow. The corresponding stellar pressure p_* is obtained from the equation of state (34), with $\rho = \rho_*$ and $T = T_*$. The velocity in the ghost zones is linearly extrapolated from the first pair of computational zones (subject to the constraint that $|v|$ does not exceed a_*), and the total energy per unit mass is evaluated using equation (36).

3.5 Cooling

Cooling in the customized VH-1 is time-split from the rest of the PPM algorithm. Across each time-step dt, a new temperature $T_j^\dagger$ in the jth zone is calculated from the current temperature T_j and density ρ_j via

$$T_j^\dagger = T_j + \frac{(\gamma - 1)\mu u}{k} \frac{\Lambda(T_j^\dagger, \rho_j) + \Lambda(T_j, \rho_j)}{2\rho_j} dt, \tag{52}$$

where $\Lambda(T, \rho)$ is the cooling rate discussed in Section 2.7. Since this equation is implicit, the code uses three-step iteration to converge toward an approximate value for $T_j^\dagger$. In zones where the temperature would drop below the stellar surface temperature T_*, it is reset to T_*; this reflects the tendency for the photospheric radiation field to keep circumstellar plasma warm. The resulting $T_j^\dagger$ values are used to update the pressure in each zone, through the equation of state (34).

4 CALCULATIONS

As an initial test of the code discussed in the preceding sections, and to explore the RFHD approach in general, we develop a model for the magnetosphere of an oblique-dipole star whose parameters (Table 1) loosely coincide with those of σ Ori E. (We stress that we are not attempting to fine tune a model for σ Ori E; however, it makes sense to begin our qualitative investigations in the same approximate region of parameter space as this archetypal star.) The mass, radius and surface temperature of the star are taken from the recent study by Krtička, Kubát & Groote (2006), with the luminosity calculated from equations (22) and (24). The wind parameters $\bar{Q}$ and α are assigned values typical to hot stars (e.g. Gayley 1995), resulting in a CAK mass-loss rate (equation 49) of $3.7 \times 10^{-9} \, M_\odot \, \text{yr}^{-1}$. The rotation period P_{rot} is based on the photometric period measured by Hesser, Ugarte & Moreno (1977), and leads to a normalized rotation

Table 1. Parameters for the RFHD simulation described in Section 4.

M_* (M$_\odot$)	R_p (R$_\odot$)	T_* (K)	L_* (L$_\odot$)	β (°)	X	Z
8.9	5.3	22 500	7420	55	0.7	0.02

$P_{\rm rot}$ (d)		α	γ	N_s	$\Delta_{\rm d}$	Δ_*
1.2	500	0.6	5/3	25	100	100

frequency $w = 0.73$. The dipole obliquity β is adopted from the RRM model presented by Townsend et al. (2005).

To piece together a 3D model for the magnetosphere, we use VH-1 to simulate the flow along a total of 1140 field lines, arranged on a grid of 60 magnetic shell parameters L and 19 magnetic azimuths $\tilde{\phi}$. The azimuth values span the $0° \leqslant \tilde{\phi} \leqslant 90°$ quadrant in 5° increments; symmetry is used to replicate the simulation results over the remaining $90° \leqslant \tilde{\phi} \leqslant 360°$ interval, effectively leading to 72 azimuthal points. The 60 values of the shell parameter are distributed according to the formula

$$\ln L = \ln 1.2 + \ln(11.2/1.2)\frac{\ell - 1}{59} \qquad (\ell = 1 \ldots 60). \tag{53}$$

This logarithmic distribution provides higher resolution close to the star, where we expect magnetospheric structure to depend more sensitively on L. The innermost, $\ell = 1$ field lines have $L = 1.2$; by comparison, the stellar equatorial radius for the adopted parameters is $R_{\rm eq} = 1.11 R_{\rm p}$. These field lines are composed of $N_s = 25$ grid zones in each of the two surface domains and – with the choices $\Delta_{\rm d}$ and Δ_* listed in Table 1 – $N_{\rm m} = 211$ zones in the intervening magnetosphere domain. The outermost, $\ell = 60$ field lines have $L = 11.2$, and therefore extend out to just over six times the Kepler corotation radius $r_{\rm K} = 1.86 R_{\rm p}$ (cf. equation A8). These field lines again have $N_s = 25$, but now the magnetosphere domain has $N_{\rm m} = 1149$ zones, ensuring a zone size $ds = 0.027 R_{\rm p}$ that is less than half the asymptotic scaleheight $h_\infty = 0.064 R_{\rm p}$ defined by equation (A9).

Each 1D simulation runs for 200 stellar rotation cycles ($\sim$21 Ms). This is significantly longer than typical flow times $\sim$20 ks, to ensure that radiative relaxation from the initial state is obtained, and to follow the long-term evolution of the magnetosphere. Since the simulations for each field line are independent, they can be distributed across different processors, computers or even clusters. In the present case, the 1140 individual simulations were run on a cluster of eight 2.0 GHz dual-core AMD Opteron nodes (for a total of 16 processors). On average, each simulation took $\sim$200 min (although there was a significant spread about this mean), giving a total computation time of $\sim$10 d.

5 RESULTS

The complete 3D magnetospheric model we describe above, composed of 1140 1D simulations, occupies $\sim$36 GB of storage. Presenting this significant data set in an informative manner poses quite a challenge. Fortunately, the independence of the individual simulations is once again of benefit, since the flow can be analysed first in one dimension, along an individual field line (Section 5.1), then in two dimensions, along field lines lying in the same meridional plane (Section 5.2) and then in three dimensions (Section 5.3), for the complete model.

5.1 1D, along individual field line

In this section, we focus exclusively on the flow along the field line having a magnetic shell index $\ell = 20$ (cf. equation 53), corresponding to $L = 2.45$, and an azimuth $\tilde{\phi} = 90°$. With these parameters, the field line extends out beyond the Kepler radius $r_{\rm K} = 1.86 R_{\rm p}$, and passes through the intersection between magnetic and rotational equators. According to the RRM model (cf. TO05), these properties should be favourable to the steady accumulation of cooled plasma at the field-line summit. This expectation is amply confirmed by Fig. 2, which shows the time evolution of ρ, T and v along the field line for the first 3 Ms of the simulation. (The dynamics during the remainder of the simulation are not significantly different from those seen toward the end of this initial time-span.) The figure should be interpreted with the aid of Fig. 3, which plots snapshots of the flow variables at four epochs of interest.

The first, 'A' snapshot shows the initial configuration described in Section 3.3. Because the velocity in both hemispheres is supersonic, reverse shocks quickly form at the magnetic equator $s = 0$, and then proceed to propagate back down the field line toward each footpoint. As wind plasma flows through these shocks it experiences an abrupt reduction in velocity, matched by corresponding discontinuous increases in density and temperature. The temperature jump, from $T = T_*$ to $T \approx 2 \times 10^7$ K, mean that the post-shock plasma cools initially with photon energies $kT \approx 2$ keV in the X-ray range.

The downward propagation of the shocks halts when the ram pressure of the pre-shock plasma matches the gas pressure in the post-shock regions. The resulting quasi-steady state, composed of standing shocks at $s = \pm 1.6 R_{\rm p}$ that enclose hot, post-shock cooling regions, is shown in snapshot 'B'. Situated at the centre of these regions is the cooled plasma predicted by the RRM model. This plasma accumulates at a local minimum of the effective potential $\Phi_{\rm eff}$ (as sampled along field lines), where it is supported in stable magnetohydrostatic equilibrium by the centrifugal force (see TO05; see also Appendix A). As we discuss further in Section 5.3, the locus formed by such potential minima resembles an azimuthally warped disc.

To characterize the behaviour of the cool disc plasma, we briefly digress to introduce the three moments:

$$\sigma_{\rm d} = \frac{1}{A_{\rm eq}} \int \rho A \, {\rm d}s, \tag{54}$$

$$s_{\rm d} = \frac{1}{A_{\rm eq}\sigma_{\rm d}} \int \rho s A \, {\rm d}s \tag{55}$$

and

$$h_{\rm d} = \left[\frac{2}{A_{\rm eq}\sigma_{\rm d}} \int \rho (s - s_{\rm d})^2 A \, {\rm d}s \right]^{1/2}, \tag{56}$$

where the integrals extend over the disc regions having $T = T_*$. These moments represent, respectively, the disc surface density (projected into the magnetic equatorial plane), the disc centroid and the disc scaleheight. When applied to the 1D simulations, the above expressions are evaluated via finite-volume equivalents:

$$\sigma_{\rm d} = \frac{1}{A_{\rm eq}} \sum \rho_j \, {\rm d}V_j, \tag{57}$$

$$s_{\rm d} = \frac{1}{A_{\rm eq}\sigma_{\rm d}} \sum \rho_j s_j \, {\rm d}V_j \tag{58}$$

and

$$h_{\rm d} = \left[\frac{2}{A_{\rm eq}\sigma_{\rm d}} \sum \rho_j (s_j - s_{\rm d})^2 \, {\rm d}V_j \right]^{1/2}, \tag{59}$$
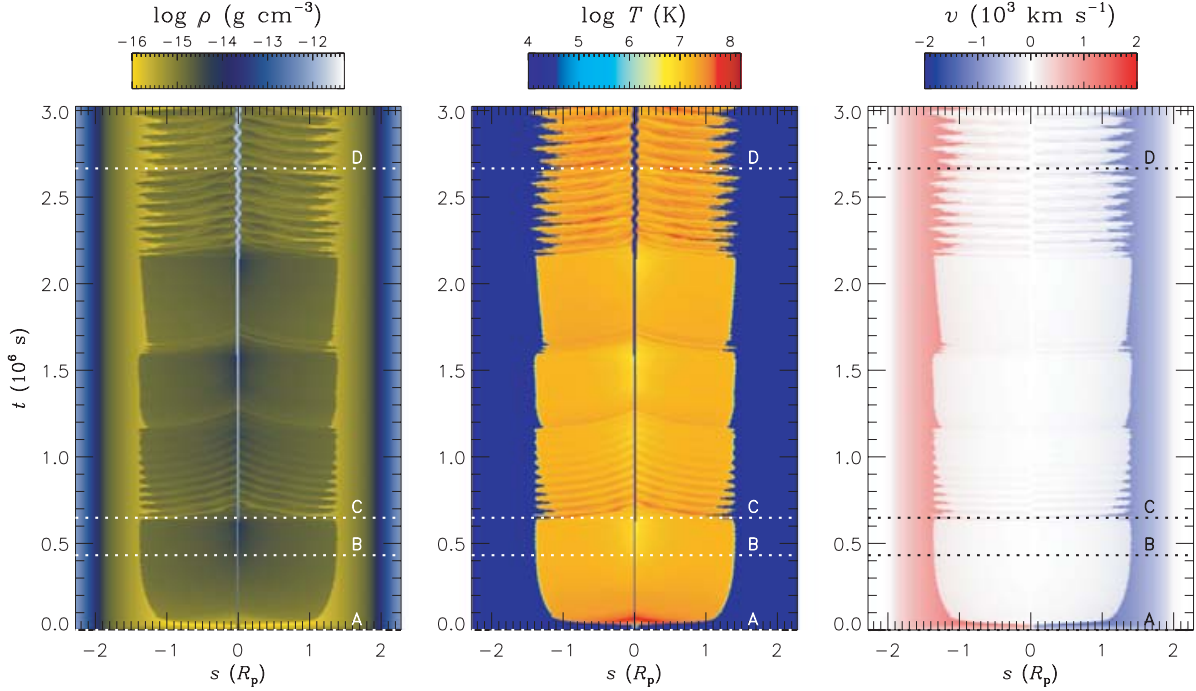
Figure 2. The time evolution of the flow along the $(L, \tilde{\phi}) = (2.45, 90°)$ field line, showing the density ρ, temperature T and velocity v as a function of arc distance s and time t. The magnetic equator is situated at $s = 0$, and the two footpoints at $s = (s_N, s_S) = (-2.28, 2.28)R_p$. The horizontal dotted lines, labelled alphabetically, show the locations of the snapshots plotted in Fig. 3; the 'A' line is situated at $t = 0$ s.
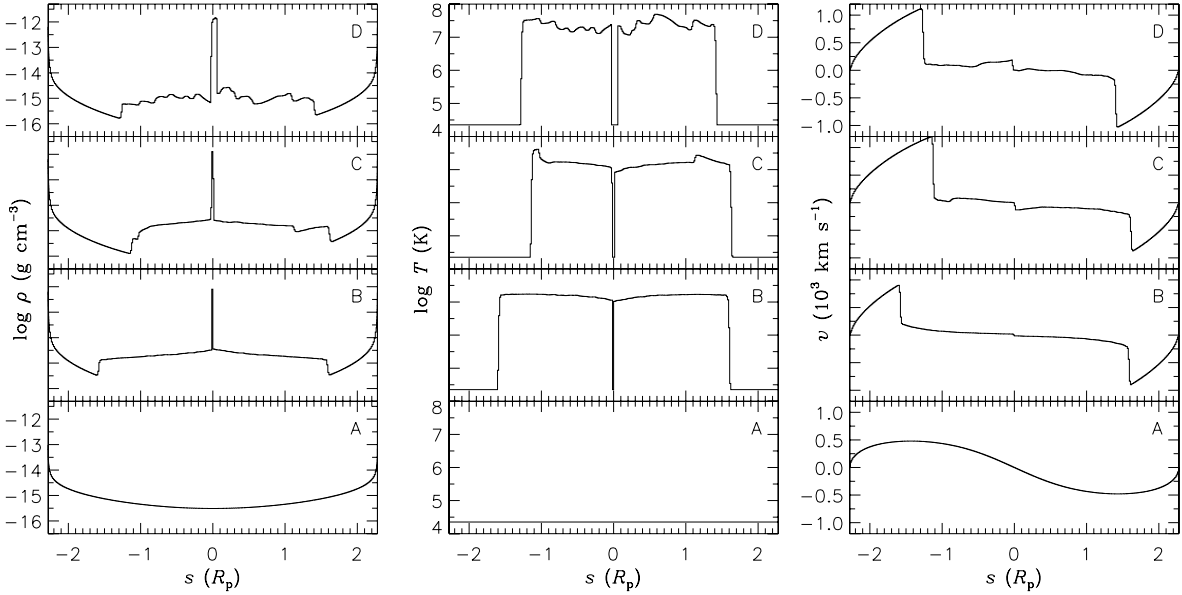

Figure 3. Snapshots of the flow along the $(L, \tilde{\phi}) = (2.45, 90°)$ field line, plotting the density ρ, temperature T and velocity v as a function of arc distance s. The times of the snapshots are indicated in Fig. 2.

where dV_j is the volume of the jth zone, and s_j the arc distance of the zone's centre. As before, the summations extend over disc zones having $T_j = T_*$.

Fig. 4 plots the moments (57–59) for the $(L, \tilde{\phi}) = (2.45, 90°)$ field line. The rightmost panel indicates that during the early stages of the simulation, the disc thickness is substantially smaller than the value $h_0 = 0.09 R_p$ predicted by the RRM model (cf. equation A6). Indeed, up until $t = 0.6$ Ms h_d is identically zero, indicating that the disc extends over only a single zone. The reason for this confinement is that the internal pressure of the cool disc is insufficient to

support it against the relatively high pressure of the hot plasma in the surrounding post-shock regions; thus, the disc becomes compressed into the smallest volume resolvable by VH-1.

This situation changes once the steady accumulation of plasma (Fig. 4, leftmost panel) raises the internal pressure to a point where the disc suddenly grows to encompass a greater number of zones. Three of these expansion events are apparent in Fig. 2, at $t = 0.6$, 1.6 and 2.1 Ms. After each event, the disc plasma undergoes oscillations back and forth about its equilibrium position $s = 0$; these are most readily seen in the centre panel of Fig. 4 for $t > 2.1$ Ms.
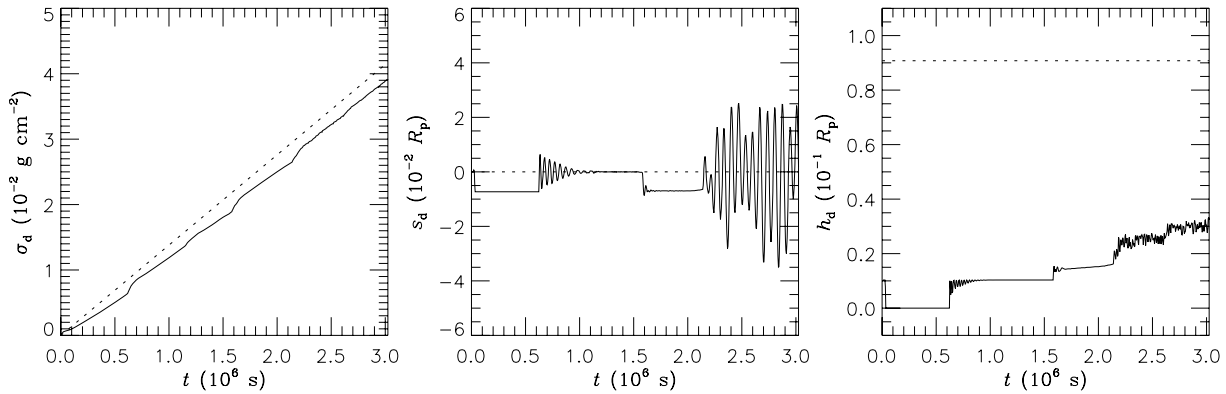
Figure 4. The surface density σ_d, centroid s_d and scaleheight h_d of the disc for the $(L, \tilde{\phi}) = (2.45, 90°)$ field line, plotted as a function of time t. The dotted lines show the corresponding predictions of the RRM model.

The oscillations are accompanied by variability of the post-shock cooling regions, involving the abrupt movement of the shock fronts toward $s = 0$, followed by a rebuilding of the cooling regions via wind feeding. Snapshot 'C' in Fig. 3 shows the state of the flow immediately after an ingress of the Northern hemisphere ($s < 0$) shock; observe how this shock is $0.45\,R_p$ closer to the disc than in snapshot 'B'. Because the density jump across a strong shock scales proportionally to the pre-shock density, this movement of the shock front translates into a reduction in the post-shock density. Thus, $\rho \approx 1.3 \times 10^{-15}\,\mathrm{g\,cm^{-3}}$ just downstream of the northern shock in snapshot 'B', but $\rho \approx 0.4 \times 10^{-15}\,\mathrm{g\,cm^{-3}}$ downstream of the shock in snapshot 'C'.

The disc oscillations after the first expansion event are damped, dying out over a time-scale ~ 0.5 Ms. The damping is even stronger for the very weak oscillations seen after the second event. Following the third event at $t = 2.1$ Ms, however, the oscillations persist at a relatively high amplitude all the way to the end of the simulation. Snapshot 'D' in Fig. 3 illustrates the flow when the oscillating disc plasma is undergoing a southward displacement ($s_d = 0.02\,R_p$).

To explore the nature of the oscillations, Appendix C develops a linear analysis of the response of the disc plasma to small-amplitude departures from stationary equilibrium. For perturbations that conserve σ_d, the analysis reveals a spectrum of normal modes having periods

$$P_m = \frac{2\pi}{\omega_m} = \pi \sqrt{\frac{2}{m}} \frac{h_0}{a_*} \qquad (m = 1, 2, 3, \ldots). \qquad (60)$$

The oscillations seen in Figs 2–4 are wholly consistent with the excitation of the dipole ($m = 1$) mode. In particular, the period $P_1 = 85.5$ ks predicted by the expression above is in good agreement with the value $P = 79.2$ ks measured from the strongest peak in the Fourier transform of the s_d data for $t > 2.1$ Ms.

What excites the dipole oscillations? In the simulations, the coincidence between the expansion events and the onset of oscillations reveals that these events impart an initial 'kick' to the disc plasma. (The kick originates because the perturbation introduced by an expansion event is usually asymmetric.) However, some other process is clearly responsible for maintaining and even amplifying the oscillations, as seen after the third expansion event at $t = 2.1$ Ms. A likely candidate for this process is the cooling instability discussed by Chevalier & Imamura (1982). These authors show that radiative cooling of thermal plasma in the temperature range $\sim 10^5$–10^7 K is linearly overstable due to the negative temperature exponent of the cooling coefficient $\mathcal{L}$. For the parameters of the cooling regions of

the $(L, \tilde{\phi}) = (2.45, 90°)$ field line, the periods of the fundamental and first-overtone unstable cooling modes are $P \approx 160$ and ≈ 40 ks, respectively,[2] bracketing the disc oscillation period $P = 79.2$ ks. This lends support to the hypothesis that a coupling between the disc modes and the cooling modes results in a global overstability, driving the disc oscillations until non-linearity leads to saturation. We intend to investigate this hypothesis further in a future paper.

To bring the present section to a close, we compare the RFHD simulation for the $(L, \tilde{\phi}) = (2.45, 90°)$ field line against the predictions of the RRM model. For the parameters specified in Table 1, the RRM model[3] predicts a rate of change $\dot{\sigma}_d = 1.38 \times 10^{-8}\,\mathrm{g\,cm^{-2}\,s^{-1}}$ for the disc surface density. Given the approximations employed in developing the model, this value is in remarkably good agreement with the empirical value $\dot{\sigma}_d = 1.31 \times 10^{-8}\,\mathrm{g\,cm^{-2}\,s^{-1}}$ derived from a linear least-squares fit to the σ_d simulation data.

To compare the distribution of disc plasma, Fig. 5 plots the density as a function of s for both model and simulation, at a time $t \approx 20.2$ Ms near the end of the simulation chosen so that the disc displacement s_d is close to zero. Once again, there is encouraging agreement between the RRM prediction and the simulation result. The only significant difference is that the wings of the Gaussian density distribution (cf. equation A5) are truncated in the simulation due to the pressure of the hot plasma in the adjacent post-shock regions.

5.2 2D, in meridional planes

We now extend the analysis to two dimensions, by considering 1D RFHD simulations all lying in the same meridional plane. Fig. 6 shows 2D images of the state of the flow at the end of the simulations, for the $\tilde{\phi} = 90°$ meridional plane. (The figure also shows images for the $\tilde{\phi} = 0°$ plane, but we defer discussion of these data until later.) The cool disc of accumulated plasma is clearly seen along the $\tilde{y}$ axis in the $\tilde{\phi} = 90°$ plane, surrounded by hot ($T \sim 10^7$–10^8 K) post-shock cooling regions. The disc does not extend all the way to the star, but is instead truncated at a radius $r = 1.8\,R_p$. Inside this radius, the centrifugal force is not strong enough to support plasma against the inward pull of gravity, and no accumulation occurs. Although

---

[2] These values are obtained from the $\alpha = -1$ eigenfrequencies tabulated by Chevalier & Imamura (1982), with $u_{in} = 900\,\mathrm{km\,s^{-1}}$ and $x_{s0} = -1.6\,R_p$.
[3] See TO05, their equation (34); in evaluating the stellar-surface field tilt μ_* appearing in this equation (and in other expressions from the RRM formalism), we take into account the stellar oblateness due to rotation, which for simplicity was neglected in the TO05 treatment.
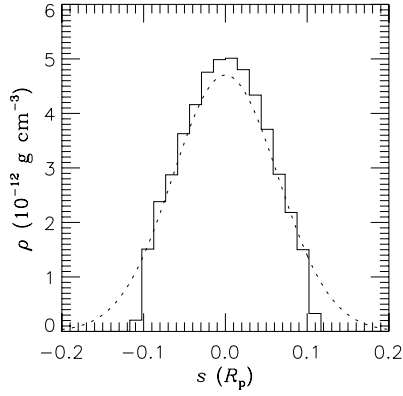
Figure 5. The density ρ in the vicinity of the cool disc, plotted as a function of arc coordinate s for the $(L, \tilde{\phi}) = (2.45, 90°)$ field line. The solid line indicates the result from the RFHD simulation at a time $t \approx 20.2$ Ms, while the dotted curve shows the prediction of the RRM model at the same t.

dense knots of plasma are formed close to the star by compression between opposing wind streams, these knots quickly slide down the magnetic field toward one or the other of the footpoints.

Fig. 7 illustrates this fallback process in a sequence of density snapshots, showing the evolution of the inner parts of the magnetosphere shortly before the end of the simulations. The white arrow in the leftmost panel indicates a knot that has formed at $(\tilde{y}, \tilde{z}) = (1.6, 0.1)\,R_p$. In the centre panel, the knot has migrated further into the northern magnetic hemisphere, and in the right-most panel begun its descent to the stellar surface. This figure is reminiscent of the infalling plasma seen in the MHD simulations

by ud-Doula & Owocki (2002, their fig. 4); in fact, the only phenomenological difference lies in the scale of the knots. Cross-field coupling in the MHD simulations allows coherence between the flow on adjacent field lines. However, this coupling is absent in the RFHD simulations (due to the neglect of the polar velocity derivative when calculating the radiative acceleration; see Section 2.5), and the scale of the knots is set therefore by the L grid spacing (cf. equation 53).

The absence of cross-field coupling is also ultimately responsible for the significant amount of structure seen in the post-shock cooling regions. If disc oscillations are excited on one particular field line, but are absent from an adjacent field line, then discontinuities in the cross-field direction appear in the flow properties, resembling a reversed letter 'C'. Thus, for instance, the $(L, \tilde{\phi}) = (3.88, 90°)$ field line in Fig. 6 has a significantly lower density than its neighbours because disc oscillations are excited on this field line, but not on the adjacent ones. As with the fallback, we expect in reality that cross-field coupling will tend to smear out such sharp discontinuities. One possible approach to including this coupling in RFHD simulations is discussed in Section 6.3.1.

Turning now to the temperature data in Fig. 6, a gradient can be seen across the post-shock regions, with the outer parts being up to an order of magnitude hotter ($T \sim 10^8$ K) than those near the star ($T \sim 10^7$ K). This gradient arises from two distinct effects. First, field lines having larger magnetic shell parameter L undergo a greater area divergence, and are therefore characterized by lower plasma densities and faster flow velocities (see Owocki & ud-Doula 2004, for a more in-depth discussion of this effect). This naturally leads to a tendency for larger L field lines to experience hotter post-shock temperatures.
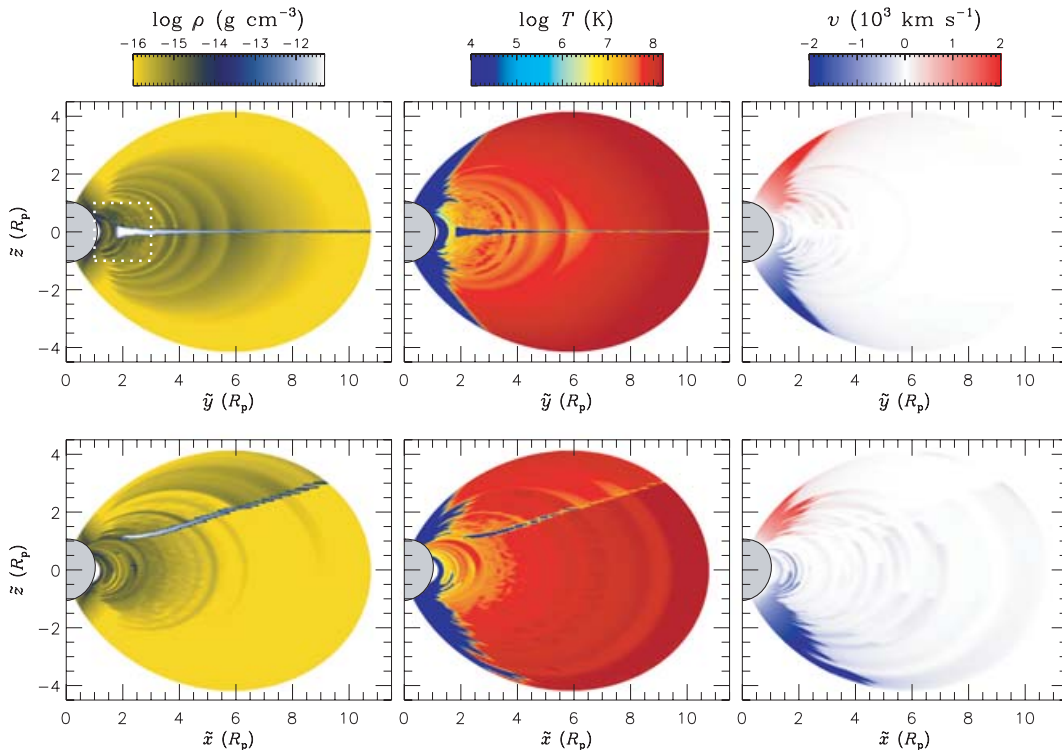

Figure 6. The state of the flow at the end of the simulations, showing the density ρ, temperature T and velocity v in the $\tilde{\phi} = 90°$ (upper row) and $\tilde{\phi} = 0°$ (lower row) meridional planes. (See Fig. 1 for a recapitulation of the geometry of these planes.) The oblate star is indicated in grey at the left-hand side of each image. Outside the regions threaded by simulation field lines (i.e. for $L < 1.2$ and $L > 11.2$), the images are left blank. The dotted rectangle in the upper left image indicates the region shown in detail in Fig. 7.
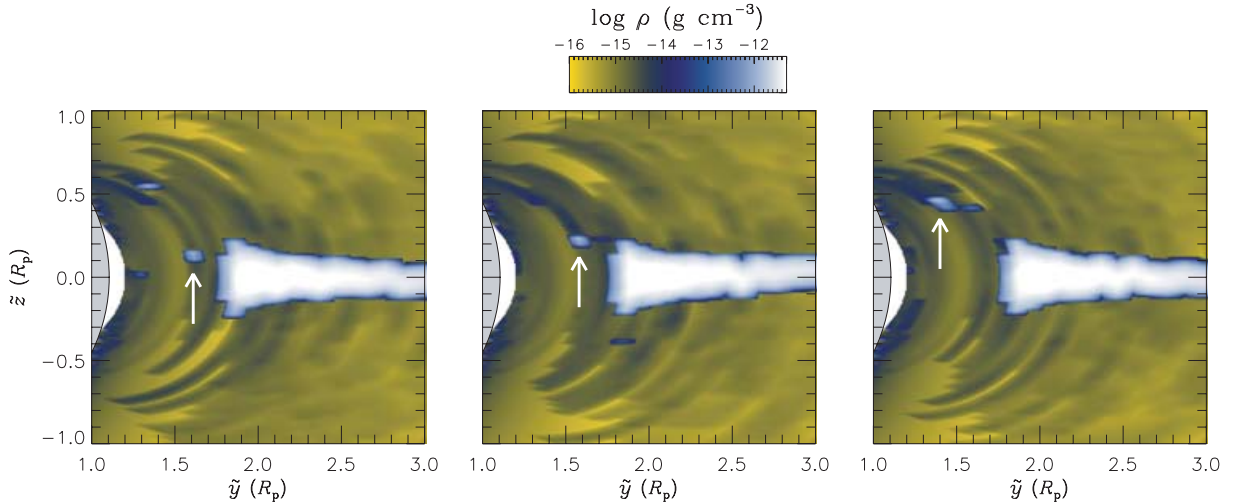
Figure 7. Snapshots of the density ρ in the inner parts of the $\tilde{\phi} = 90°$ meridional plane (see the dotted rectangle in Fig. 6), at a time $t \approx 20.4$ Ms near the end of the simulations (left), and then at increments of one quarter (centre) and one half (right) of a rotation cycle later. The white arrows indicate the location of the dense knot discussed in the text. As in Fig. 6, the star is indicated in grey at the left-hand side of each image.

Second, in a process first conjectured by Babel & Montmerle (1997a), the post-shock plasma can be pushed to even higher temperatures by the action of the centrifugal force. To accumulate on to the cool disc, the plasma must first descend to the bottom of the effective potential well (Section 5.1). The consequent release of centrifugal potential energy heats the plasma, by an amount that ultimately depends on the distance from the rotation axis. In the $\tilde{\phi} = 90°$ data shown in Fig. 6 this effect raises the plasma temperature on the outer, $L = 11.2$ field line from $T = 1.1 \times 10^8$ K at the shocks to $T = 1.8 \times 10^8$ K adjacent to the disc.

The centrifugal heating in the post-shock regions competes against cooling by atomic and inverse Compton processes (cf. Section 3.5). Initially, the centrifugal effect dominates because plasma densities are so low that atomic cooling (a ρ^2 process; see equation 38) is exceedingly inefficient. However, this situation is subsequently reversed; as plasma moves downstream of the shocks, the density eventually becomes high enough for atomic processes to cool it rapidly, in thin layers on either side of the disc (see Section 5.3). During this process, inverse Compton cooling is relatively unimportant; at low densities it is more efficient than atomic cooling, but it never becomes the dominant term on the right-hand side of the energy conservation equation (3).

Although the foregoing discussion focuses on the flow in the $\tilde{\phi} = 90°$ meridional plane, it generally applies to other meridional planes. However, one significant exception concerns the location of the cool disc. The $\tilde{\phi} = 0°$ images in Fig. 6 reveal that the disc is not symmetric about the magnetic axis, as one might presume from considering the $\tilde{\phi} = 90°$ images on their own. Rather, the disc is warped in the azimuthal direction. To explain this notion, let $\tilde{\theta}_d$ denote the centroid magnetic colatitude of the disc, obtained by setting $s = s_d$ in equation (8) and solving for $\tilde{\theta}$. Then, in a given meridional plane the disc lies approximately along a straight ray emanating from the origin, with $\tilde{\theta}_d$ remaining constant as L is varied. However, $\tilde{\theta}_d$ changes from plane to plane, resulting in azimuthal warping; for instance, $\tilde{\theta}_d \approx 70°$ in the $\tilde{\phi} = 0°$ meridional plane, whereas $\tilde{\theta}_d \approx 90°$ for the $\tilde{\phi} = 90°$ case. This warping is one of the key predictions of the RRM model, and its origin is discussed in greater detail by TO05.

In addition to revealing the disc warping, the $\tilde{\phi} = 0°$ images in Fig. 6 also illustrate a novel flow phenomenon. On a number of the innermost ($L \lesssim 1.8$) field lines, the northern reverse shock propagates back down to the stellar surface. This leads to a siphon configuration, in which plasma flows unidirectionally from the southern magnetic footpoint to the corresponding northern footpoint. (The direction of the flow is set by the relative location of the rotation axis; in the $\tilde{\phi} = 180°$ meridional plane, north-to-south siphon flows occur.) Because the southern reverse shock remains intact, part of the siphon flow is composed of shock-heated plasma at $T \approx 5 \times 10^6$ K; this plasma is relatively dense due to its proximity to the star, and therefore makes a significant contribution to the soft X-ray emission from the magnetosphere (see Section 5.3).

As with the 1D analysis in Section 5.1, we bring the present section to a close by comparing the RFHD simulation results against the predictions of the corresponding RRM model. Fig. 8 plots the disc surface density σ_d in the $\tilde{\phi} = 90°$ meridional plane, at the end of the simulations and for the model. The agreement between the two is once again very encouraging, especially in the innermost regions of the disc. In the outer regions, the simulations predict a rather smaller surface density ($\sim$10–25 per cent) than the RRM model. This modest discrepancy appears correlated with the observation that, for field lines having $L \gtrsim 6$, the disc remains confined to a single zone – no expansion events occur on these field lines over the duration of the simulations.

5.3 Full 3D model

Having examined the results of the RFHD simulations for an individual field line, and for field lines lying in meridional planes, we now turn to the complete, 3D picture. Fig. 9 shows images of the proton column density N_p at the end of the simulations, viewed from six equally spaced rotational azimuths spanning the range $0° \leqslant \phi \leqslant 180°$ (the remaining interval $180° \leqslant \phi \leqslant 360°$ is mirror symmetric through the vertical axis). Following Townsend et al. (2005), a viewing inclination $i = 75°$ with respect to the rotation axis is adopted. The column density is calculated from ray integrals
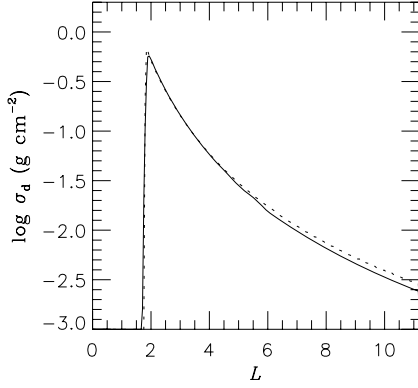
Figure 8. The disc surface density σ_d in the $\tilde{\phi} = 90°$ meridional plane, plotted as a function of magnetic shell parameter L. The solid line shows the final state at the end of the RFHD simulations, while the dotted line indicates the corresponding prediction of the RRM model.

of the form

$$N_p = \int n_p \, dz_i, \tag{61}$$

where z_i is the perpendicular distance to the image plane, and the proton number density n_p was defined in equation (39). The mass density ρ appearing in this latter equation is calculated using trilinear interpolation from the $(s, L, \tilde{\phi})$ field-line coordinate system on to the (x_i, y_i, z_i) Cartesian image coordinate system. Along rays that intersect the star, the integral is truncated at the stellar surface.

The figure clearly illustrates the 3D structure of the dense, corotating disc discussed in previous sections. (The plasma in the wind and post-shock regions is effectively invisible, since it is orders-of-magnitude less dense than that composing the disc.) This disc possesses three important characteristics predicted by the RRM model. First, it has an average inclination that lies somewhere between the magnetic and rotational equatorial planes. Second, it exhibits a hole at its centre. Third, the surface density across the disc is non-uniform, with the plasma concentrated into two elongated 'clouds' situated at the intersection between magnetic and rotational equators. These clouds are best seen in the $\phi = 180°$ panel of the figure. In the case of σ Ori E, the existence of such clouds has been inferred from Hα measurements (e.g. Groote & Hunger 1982; Bolton et al. 1987), and Townsend et al. (2005) have demonstrated how the clouds are simultaneously responsible for the distinctive spectroscopic and photometric variability exhibited by the star.

To explore further the degree of correspondence with the RRM model, Fig. 10 plots the quantities

$$R(\sigma_d) = \frac{\sigma_{d,RFHD}}{\sigma_{d,RRM}} \tag{62}$$

and

$$\Delta(\tilde{\theta}_d) = \tilde{\theta}_{d,RFHD} - \tilde{\theta}_{d,RRM} \tag{63}$$

in the $\tilde{x}-\tilde{y}$ magnetic equatorial plane, where the subscripts $_{RFHD}$ and $_{RRM}$ denote values obtained from the RFHD simulations and the RRM model, respectively. These quantities represent the ratio of disc surface densities σ_d, as defined by equation (54), and the difference in the disc centroid colatitudes $\tilde{\theta}_d$ introduced in Section 5.2.

The figure reveals that once again the agreement between simulations and model is good. The maximum differences in surface density are below the 25 per cent level, and – as already discussed – are strongly correlated with those disc regions that have not undergone any expansion events. The differences in centroid colatitude angle

do not rise above a few degrees; they tend to be most positive around $\tilde{\phi} = 0°$, and most negative around $\tilde{\phi} = 180°$, so the RFHD disc is slightly closer to the magnetic equatorial plane than the RRM disc. Based on these findings, we can conclude that the disc plasma distribution predicted by the RRM model furnishes a close approximation to the distribution determined via the physically more sophisticated (yet computationally more expensive) RFHD approach.

Of course, the significant caveat here is that the RRM model is limited to consideration only of the cool plasma in the disc. Whereas, the RFHD simulations also encompass the hot post-shock plasma responsible, for instance, for magnetospheric X-ray emission. To illustrate the spatial and thermal distribution of this plasma, we introduce a two-temperature emission measure density (EMD):

$$\mathcal{E}(T_1, T_2) = \int_{T_1}^{T_2} \left[\int n_e n_p \delta(T - T') \, dz_i \right] dT', \tag{64}$$

where $\delta()$ is the Dirac delta function, and n_e is the electron number density (cf. equation 11). The EMD characterizes the radiative recombination emission by plasma in the temperature range $T_1 < T < T_2$. Fig. 11 shows images of $\mathcal{E}$ at the end of the simulations, for the 'face on' ($\phi = 0°, 180°$) and 'edge-on' ($\phi = 108°$) viewing aspects, and for temperature ranges that correspond to thermal emission at optical/UV ($T < 10^5$ K), extreme UV ($10^5 < T < 10^6$ K), soft X-ray ($10^6 < T < 10^7$ K) and hard X-ray ($T > 10^7$ K) energies.

The optical/UV images confirm the concentration of Hα-emitting plasma into two clouds. However, at higher temperatures a different distribution emerges. In the EUV range, the plasma is situated primarily in thin cooling layers on either side of the disc. Because the cooling from 10^6 to 10^5 K is so efficient (on account of the large number of metal lines available), these layers are underresolved in the simulations, and appear fragmented into many small islands of emission. Similarly fragmented cooling layers are seen in the outer parts of the soft X-ray EMD images, but the preponderance of the emission in this $10^6 < T < 10^7$ K range comes from a toroidal belt surrounding the star. This belt is primarily composed of the hot, dense plasma associated with the siphon flows discussed in Section 5.2 (and also see Fig. 6).

The soft X-ray belt is enclosed by a torus of hard X-ray emission, seen in the $T > 10^7$ K images to extend out to about $4R_p$. Beyond this radius, an asymmetry develops on either side of the disc, with those field lines that pass near the rotational poles showing much weaker emission than those that avoid the poles. This asymmetry is most evident in the $\phi = 108°$ (edge-on) panel; observe how the emission is strongest in the northern magnetic hemisphere on the left-hand side of the image, but vice versa on the right-hand side. The origin of the asymmetry can be seen in the $\tilde{\phi} = 0°$ images of Fig. 6; note the significant difference in the density of the post-shock regions on either side of the disc, which translates directly into the $\mathcal{E}$ asymmetry. The density difference itself arises as a result of the positioning of the shock fronts; the disc in the $\tilde{\phi} = 0°$ meridional plane is situated in the northern magnetic hemisphere, and the shock fronts in this hemisphere are closer to the stellar surface, implying a higher density in the post-shock region.

To complete our discussion of the magnetospheric emission, we consider the differential emission measure (DEM) distribution:

$$\mathcal{D}(T) = \frac{d}{d \ln T} \left[\int \int \mathcal{E}(0, T) \, dx_i \, dy_i \right]. \tag{65}$$

Fig. 12 plots $\mathcal{D}$ as a function of temperature, for the $\phi = 0°$ case shown in Fig. 11. The figure reveals an essentially bimodal DEM distribution, with a narrow peak at $T = 22\,500$ K $= T_*$ corresponding
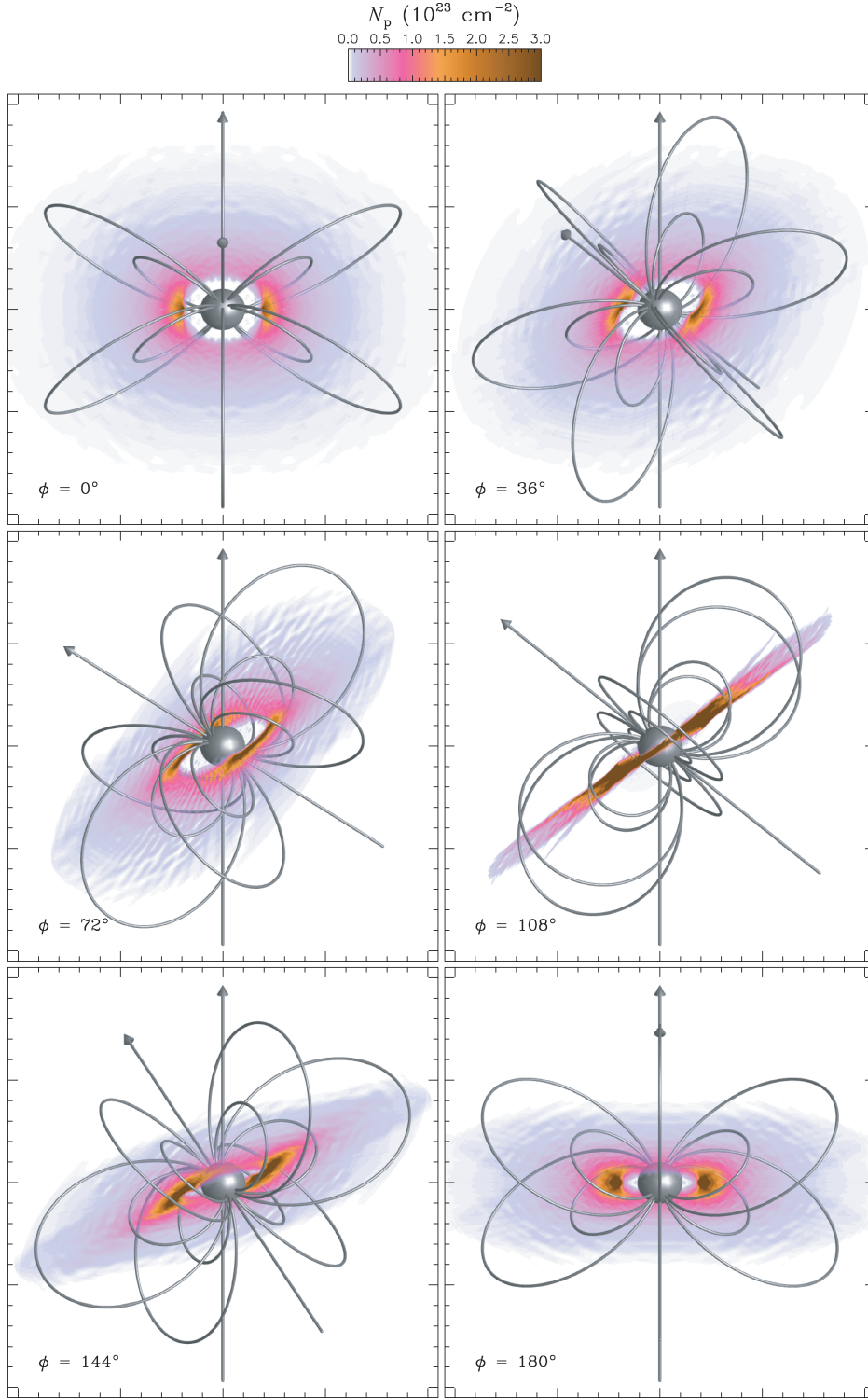
N_{p} $(10^{23}\ \mathrm{cm}^{-2})$

0.0 0.5 1.0 1.5 2.0 2.5 3.0

Figure 9. The proton column density N_{p} at the end of the simulations, viewed from six different rotational azimuths ϕ. The oblate star is shown in grey at the centre of each panel, arrows indicate the magnetic and rotation axes (the latter being the vertical, fixed one) and the curved arcs show field lines having magnetic shell parameters $L = 5, 10$ and magnetic azimuths $\tilde{\phi} = 0°, 60°, 120°, \ldots, 300°$.

to the cool disc plasma, and a broad peak centred at $T \approx 4 \times 10^7$ K associated with the extended regions of hard X-ray emission seen in the topmost images of Fig. 11. These regions are not subject to any appreciable occultation by the star, and as a consequence there is almost no change to the X-ray peak seen in Fig. 12 as the rotational azimuth ϕ is varied.

6 DISCUSSION

The analysis in preceding sections is largely directed toward comparing the results from the RFHD simulations against the corresponding predictions of the RRM formalism. This comparison confirms that the two complementary frameworks for modelling
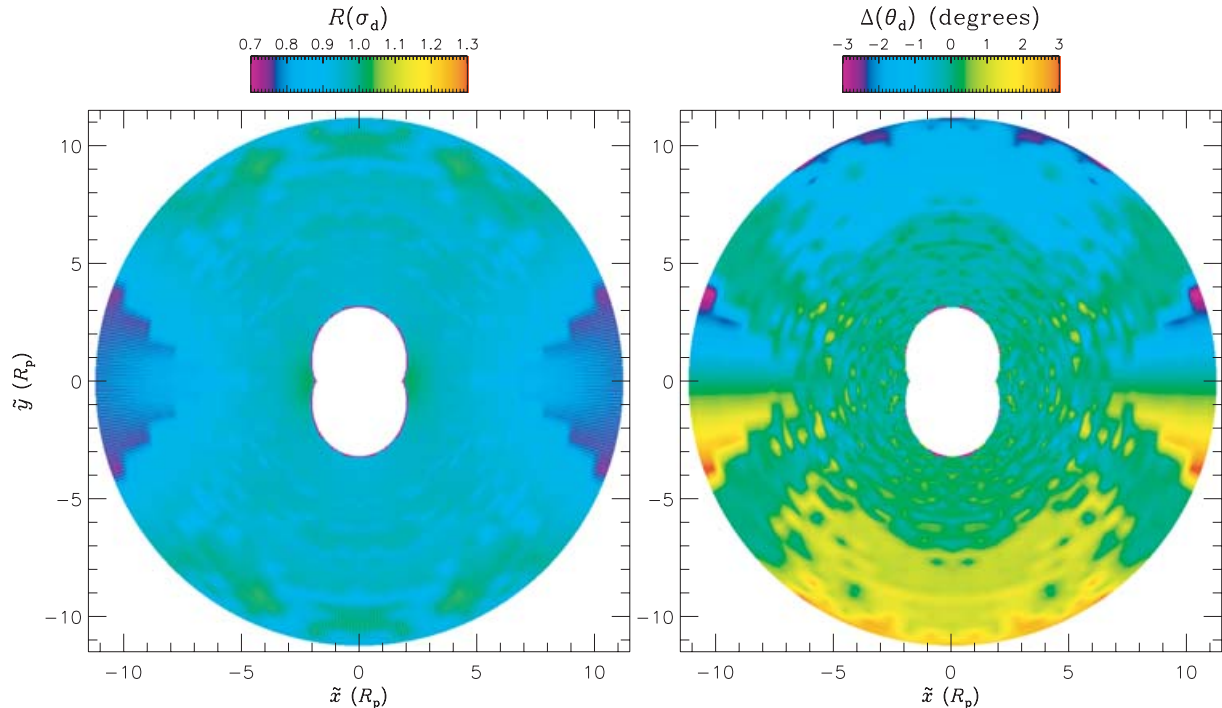
Figure 10. The surface density ratio (left) and centroid colatitude difference (right) between the RFHD simulations and the RRM model, across the magnetic equatorial ($\tilde{x}$–$\tilde{y}$) plane.

massive-star magnetospheres are in good agreement. However, the RFHD approach has a far broader scope than the RRM model, and we have only begun to explore its potential applications. Our preliminary investigation of a σ Ori E-like star has already revealed a variety of novel phenomena, such as disc oscillations and centrifugal heating. In Section 6.2 we discuss the prospects for the next logical step of comparing RFHD simulations against observations of magnetic stars. In Section 6.3, we review the limitations of the RFHD approach, and suggest how these might be overcome in future studies. First, however, we examine the relationship between RFHD and previous work.

6.1 Relation to previous work

The RFHD approach presented in this paper has allowed (to our knowledge) the first ever time-dependent, 3D simulation of a massive-star magnetosphere. In developing the new approach, we have drawn extensively on previous investigations of stellar magnetospheres. From the perspective of disc accumulation, these include the RRM model (TO05), and the earlier rigid-field models advanced by Michel & Sturrock (1974) and Nakajima (1985). From the perspective of wind dynamics, the key narrative has been the MCWS paradigm of Babel & Montmerle (1997a).

Indeed, the modelling strategy employed by Babel & Montmerle (1997a) directly foreshadows the RFHD approach, and a comparison between the two is appropriate. These authors also adopt a rigid-field ansatz, and likewise cast the flow in terms of independent 1D hydrodynamical problems that include the effects of rotation and radiative cooling. However, they restrict their analysis to the 2D axisymmetric case of an aligned dipole ($\beta = 0°$), and instead of constructing global solutions they treat the wind, post-shock and disc regions separately, combining them in a post hoc step based on matching conditions. Moreover, rather than using a hydrodynami-

cal code they treat the flow in the wind and post-shock regions by stationary integration of the time-independent momentum equation. This rules out any possibility of simulating dynamical phenomena such as disc oscillations or the fallback of material close to the star.

For these reasons, we regard the RFHD approach as a significant advance beyond the MCWS model that augured it. What of other treatments? As discussed in the Introduction, MHD simulations (e.g. ud-Doula & Owocki 2002) tend to be impractical when field lines become almost rigid. Therefore, the direct overlap between MHD and RFHD is naturally limited – although this may change if the RFHD approach can successfully be extended to open field topologies, as is discussed in Section 6.3.3. Even for stars accessible to MHD simulation, the RFHD approach will retain some advantage due to its relatively low computational costs.

6.2 Comparison with observations

In presenting the results from the 3D magnetosphere model (Section 5), we avoid any specific comparison with observations. This reflects the focus of the paper toward introducing the RFHD approach and exploring the physical processes at work in massive-star magnetospheres. Here, we outline those specific areas where we believe a confrontation between models and observations will prove most fruitful. However, apart from brief remarks on the correspondence of our results to recent and historical observations, we defer the detailed quantitative modelling to subsequent papers.

Townsend et al. (2005) have already found that the RRM model furnishes a good agreement to the Hα and photometric variability of σ Ori E. Since the RFHD simulations predict a disc plasma distribution similar to the RRM model (cf. Section 5.3), the improvements brought by the simulations – at optical wavelengths – are likely to be incremental. Nevertheless, the radiative transfer treatment adopted by Townsend et al. (2005) is at the simplest possible level, and lacks
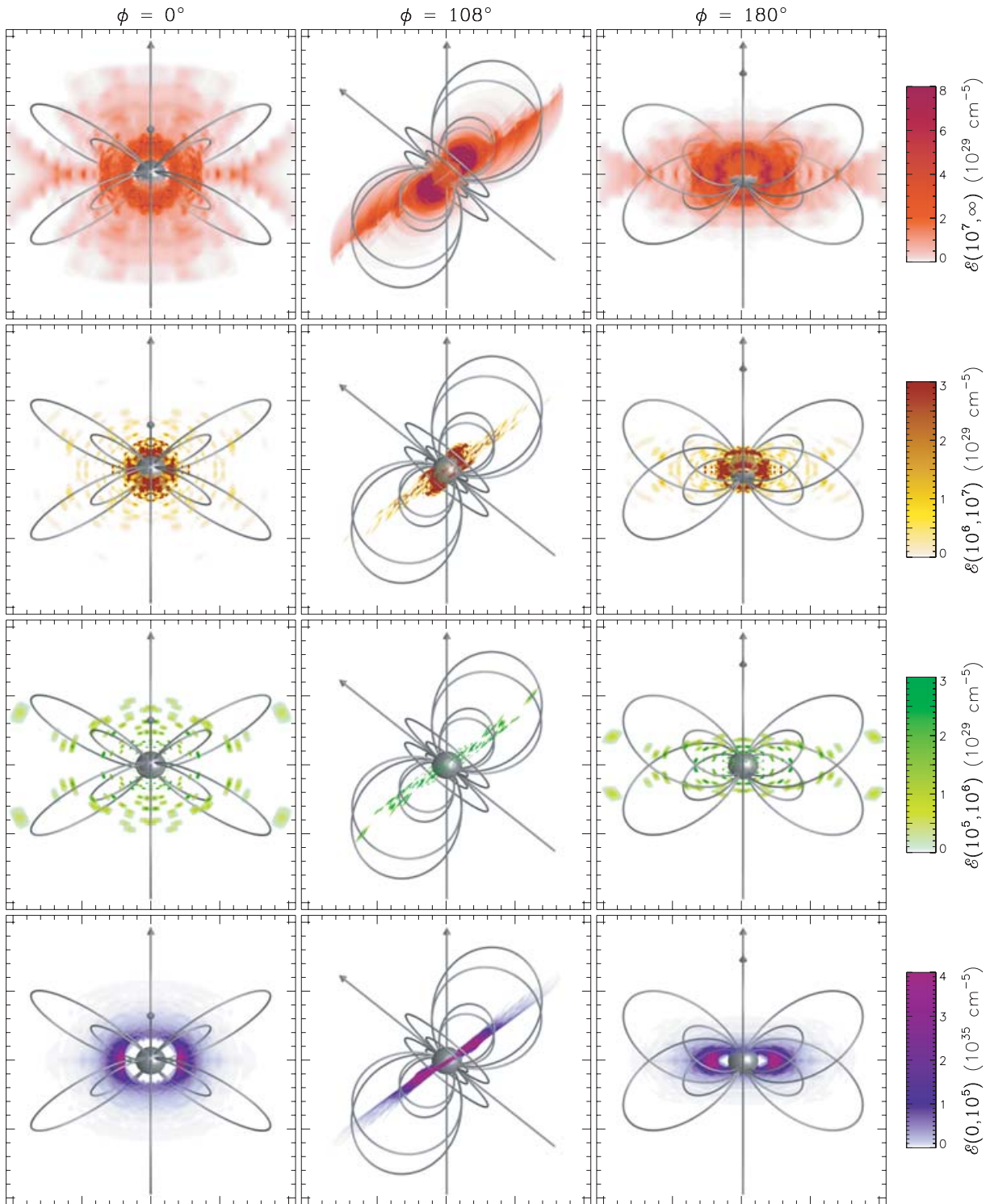
Figure 11. The EMD $\mathcal{E}(T_1, T_2)$, viewed from three different rotational azimuths ϕ, and for four temperature ranges (T_1, T_2) corresponding (top-to-bottom) to hard X-ray, soft X-ray, EUV and optical/UV emission. The star, axes and field lines are the same as in Fig. 9.

a realistic treatment of atomic physics. Thus, there is ample room for progress in this area.

The scope for progress is greater at other wavelengths, however. In their *Chandra* survey of M17, Broos et al. (2007) uncovered a population of B0-B3 stars characterized by hard (up to ~5 keV) X-ray emission. The DEM distributions presented in Section 5.3 are generally consistent with this level of hardness, suggesting a

magnetic wind-shock origin for the B stars' X-rays. To test this hypothesis at a qualitative level, the RFHD simulations can be combined with standard emission codes such as APEC (Smith et al. 2001) to synthesize spectra for direct comparison against the observations.

Such modelling should also help to understand the X-ray emission of known-magnetic Bp stars. Some of these are notable on account of the absence of any significant X-ray detections (see
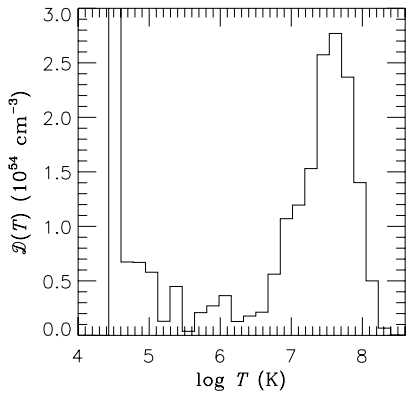
Figure 12. The DEM distribution $\mathcal{D}$, plotted as a function of temperature T for the $\phi = 0°$ case shown in Fig. 11. The ordinate scale is chosen to emphasize the emission at EUV and X-ray energies; the truncated peak at low temperatures extends up to $\approx 2 \times 10^{60} \, \mathrm{cm}^{-3}$.

e.g. Drake et al. 1994; Czesla & Schmitt 2007). In the case of σ Ori E X-rays are seen, but they show an ambiguous character: a two-temperature fit to *Chandra* measurements gives $kT \approx$ 0.7, 2.2–3.8 keV (Skinner et al. 2004), whereas a corresponding fit to *XMM–Newton* data finds $kT \approx 0.3$, 1.1 keV (Sanz-Forcada, Franciosini & Pallavicini 2004). The RFHD simulations based loosely on the parameters of σ Ori E predict a non-varying and rather harder spectrum, with a DEM distribution peaking around $kT \approx 3.5$ keV (cf. Fig. 12). This harder-than-observed spectrum could be a consequence of our neglect of thermal conduction (cf. Section 2.7). Alternatively, it could be that the mass-loss rate adopted in the simulations is too high. (A larger $\dot{M}$ leads to a higher density wind, which in turn pushes the shocks further from the star where the flow velocity is higher.) In this respect, we note that there is mounting evidence from a number of independent diagnostics that mass-loss rates of OB stars have historically been overestimated (see e.g. Smith & Owocki 2006, and references therein).

At radio wavelengths, the emission properties of magnetic Bp stars are rather more consistent than for X-rays. However, the physical mechanisms responsible remain somewhat controversial (e.g. Drake 1998). In a recent paper, Trigilio et al. (2004) advance a 3D model incorporating gyrosynchrotron emission from mildly relativistic electrons accelerated in an equatorial current sheet. This current sheet lies outside the inner, rigid-field regions of the magnetosphere, and cannot be modelled directly using the RFHD approach (although see Section 6.3.3). However, Trigilio et al. (2004) suggest that the thermal plasma trapped in the post-shock cooling regions of the inner magnetosphere plays an important role in modulating (via free–free absorption) the radio emission. The RFHD approach will prove useful in testing this idea.

At UV wavelengths, there is good potential for headway to be made. A number of magnetic massive stars were observed extensively by *International Ultraviolet Explorer* (*IUE*; see Smith & Groote 2001, and references therein), leading to empirical models for equatorially focused wind streams (e.g. Shore & Brown 1990) that prefigured the MCWS model. In the case of σ Ori E and similar He-strong stars, Smith & Groote (2001) find that the strengths of UV lines are consistent with absorbing column densities of 10^{22}–$10^{23} \, \mathrm{cm}^{-2}$. Allowing for the fact that these authors assumed a covering factor of 100 per cent (whereas magnetospheric discs are in fact closer to 10 per cent), such values are consistent with the $N_p \approx 3 \times 10^{23} \, \mathrm{cm}^{-2}$ column densities found in the RFHD simu-

lations. The task now is to investigate whether the simulations can reproduce the detailed absorption profiles measured by *IUE*.

On a more speculative note, the RFHD approach may be able to shed some light on particle acceleration processes around massive stars. Bell (1978a,b) and Blandford & Ostriker (1978) independently suggested that Fermi acceleration of particles in astrophysical shocks could explain the cosmic-ray energy spectrum up to the 'knee' at $\sim 10^6$–10^7 GeV. Typically, supernova remnants are considered the most likely locations for this to occur (Stanev 2004). However, it seems possible that the circumstellar environments of strong-field massive stars could also be sites for particle acceleration. Babel & Montmerle (1997a) suggest that the highly sub-Alfvénic nature of the magnetically channelled wind shocks (due to the near-rigid field) means that the second-order Fermi process should be effective. They claim that relativistic electrons produced in this manner can explain the radio emission from magnetic massive stars, without the need for the current sheets invoked by Trigilio et al. (2004).

We conjecture that the same mechanism operating on protons and/or ions (which are far less sensitive to inverse Compton losses than electrons) might ultimately lead to the production of energetic γ-rays. With recent advent of high-sensitivity ground-based Cherenkov telescopes such as HESS (High Energy Stereoscopic System; Hinton 2004) and VERITAS (Very Energetic Radiation Imaging Telescope Array System; Holder 2006), which have the sensitivity and angular resolution to detect these γ-rays, theoretical progress on this issue would be particularly timely.

6.3 Limitations

To bring the discussion to a close, we briefly review the present limitations of the RFHD approach, and (where possible) suggest how these limitations might be overcome in future extensions to the basic approach.

6.3.1 Cross-field coupling

In deriving the adopted expression (33) for the radiative acceleration $\boldsymbol{g}_{\mathrm{rad}}$, the polar velocity derivative $(\partial v / \partial \tilde{\theta})_{\tilde{r}}$ is neglected. Although the approximation is generally quite reasonable, it necessarily suppresses any coupling between the flow on adjacent field lines that may be important in setting the scale of knots and cross-field discontinuities (Section 5.2).

To include this coupling, we contemplate an extension to the basic RFHD approach that involves conducting the 1D simulations lying in the same meridional plane in parallel. By this, we mean that each numerical time-step advances the flow data of all coplanar field lines together. This way, the necessary velocity data to calculate $(\partial v / \partial \tilde{r})_{\tilde{\theta}}$ are available throughout the simulation, and it is not necessary to make the approximation (30). The additional computational costs of performing the 1D simulations in parallel are quite reasonable; beyond the additional memory overhead, the only significant issue is that the numerical time-step is limited by the Courant criterion as applied to all field lines together. This means that the simulations advance at the rate of the 'slowest' (shortest Courant time) field line.

6.3.2 Rigid-field ansatz

A key ingredient of the RFHD approach is the ansatz that field lines remain rigid. This applies as long as the magnetic Lorentz force can balance any competing forces acting perpendicular to field

lines with only minimal distortion from the assumed unstressed configuration, taken here to be a dipole. In the wind outflow regions, the relevant competition can be characterized in terms of the global wind magnetic confinement parameter, η_*, defined by ud-Doula & Owocki (2002). These authors' MHD simulations show that the Alfvén radius – where closed field lines become opened into a radial configuration by the wind – scales as $r_A \approx \eta_*^{1/4} R_*$.

The parameters adopted for the RFHD simulations (cf. Table 1), together with a polar field strength $\sim 10^4$ G corresponding to the value inferred for σ Ori E (Landstreet & Borra 1978), imply a global confinement parameter $\eta_* \approx 10^7$. The conclusion is therefore that the wind should substantially distort field lines only for radii $r \gtrsim r_A \approx 50 R_*$ – significantly further out than the maximum shell parameter $L = 11.2$ considered in our simulations. Although this simple analysis does not account for the presence of shocks, or for the effects of the Coriolis force, these additional processes can be expected to incur modest (order-unity) modifications to the total flow energy. Hence, their inclusion should not appreciably modify the basic η_*-based analysis for the overall competition between field and flow in regions outside the disc.

However, the radial increase of the centrifugal force makes it a potentially important limiting factor in a rigid-field approach, particularly for the secularly accumulating plasma in the outer regions of the disc. In fact, as discussed in the appendix of TO05, the centrifugal force acting on this plasma should eventually become stronger than the available magnetic tension, leading to the kind of centrifugally driven breakout seen in the MHD simulations of ud-Doula, Townsend & Owocki (2006). The time-scale for breakout decreases sharply with local disc radius, asymptotically as r^{-4}; moreover, the overall normalization of this time-scale scales with a disc confinement parameter that is quite analogous to, and has a similar magnitude to, the wind parameter η_* (see e.g. TO05, their equations A7 and A8).

In the RFHD simulations, and again adopting the inferred field strength for σ Ori E, the outermost, $L = 11.2$ field line has a disc breakout time of ≈ 2 Ms, roughly an order of magnitude shorter than the simulation duration. Indeed, over this duration all field lines having $L \gtrsim 6$ should undergo one or more breakout episodes, thus formally violating the rigid-field ansatz when applying the RFHD simulations of these outer regions to σ Ori E. However, in practice these regions make only a minor contribution to the disc emission (cf. the lower images of Fig. 11), implying that the model should still be applicable for interpreting optical line diagnostics like Hα. Moreover, once field lines reconnect after a breakout event, the wind shocks should quickly reform to nearly their characteristic asymptotic strength, meaning that the associated X-ray emission signatures are also likely to be only weakly affected. While further direct MHD simulations would be helpful in testing these expectations, it seems that models based on the rigid-field ansatz here still provide good approximate predictions of key observational diagnostics.

6.3.3 *Open field topologies*

Recall that the general RFHD approach is not necessarily limited to any particular magnetic topology, such as the dipole form adopted here. It merely requires that this topology be pre-specified and independent of the actual flow. For example, the basic approach could even be applied to a topology in which a dipole field is opened into a radial configuration in the region outside the Alfvén radius. Physically such opening occurs because of the stresses of wind outflow,

but phenomenologically it can be pre-specified by invoking current sheets (e.g. Connerney, Acuna & Ness 1981; Tsyganenko 1989; Tsyganenko & Peredo 1994) and/or source surfaces (e.g. Altschuler & Newkirk 1969) for regions above r_A. In models of the solar wind, the recent investigation by Riley et al. (2006) confirms that such source-surface methods lead to global field topologies that are in good agreement with full MHD solutions.

In the context of massive stars, corresponding open-field RFHD simulations could provide a first attempt toward a 3D model for the effects of the field on open regions of wind outflow. Although not contributing appreciably to optical or X-ray emission, the inclusion of such outflow regions in an RFHD model could prove a good initial basis for synthesizing phase-dependent UV wind absorption profiles, for comparison against archival *IUE* spectra.

7 SUMMARY

We have presented a new RFHD approach to modelling massive-star magnetospheres. Within the rigid-field ansatz, the flow along each field line is treated as an independent 1D hydrodynamical problem. Using the VH-1 code, we performed many separate 1D simulations of differing field lines, and pieced them together to build up 3D model of a σ Ori E-like star.

These results from these simulations showcase the potential of the RFHD approach, both by confirming the findings of previous studies (e.g. wind collision shocks, disc accumulation) and by revealing new phenomena (e.g. disc oscillations, siphon flows, centrifugal heating). Hence, we anticipate that the new approach will prove a powerful tool in future investigations of massive-star magnetospheres.

REFERENCES

Abramowitz M., Stegun I. A., 1972, Handbook of Mathematical Functions. Dover Press, New York
Airapetian V. S., 2000, in Smith M. A., Henrichs H. F., Fabregat J., eds, IAU Colloq. 175, The Be Phenomenon in Early-Type Stars. p. 334
Altschuler M. D., Newkirk G., Jr, 1969, Sol. Phys., 9, 131
Babel J., Montmerle T., 1997a, A&A, 323, 121
Babel J., Montmerle T., 1997b, ApJ, 485, L29
Bandiera R., Chen Y., 1994, A&A, 284, 629
Bell A. R., 1978a, MNRAS, 182, 147
Bell A. R., 1978b, MNRAS, 182, 443
Blandford R. D., Ostriker J. P., 1978, ApJ, 221, L29
Bolton C. T., Fullerton A. W., Bohlender D., Landstreet J. D., Gies D. R., 1987, in Slettebak A., Snow T. P., eds, IAU Colloq. 92, Physics of Be Stars. Cambridge University Press, Cambridge, p. 82
Borra E. F., Landstreet J. D., 1979, ApJ, 228, 809
Borra E. F., Landstreet J. D., Thompson I., 1983, ApJS, 53, 151
Broos P. S., Feigelson E. D., Townsley L. K., Getman K. V., Wang J., Garmire G. P., Jiang Z., Tsuboi Y., 2007, ApJS, 169, 353
Castor J. I., Abbott D. C., Klein R. I., 1975, ApJ, 195, 157 (CAK)
Charbonneau P., MacGregor K. B., 2001, ApJ, 559, 1094
Chevalier R. A., Imamura J. N., 1982, ApJ, 261, 543
Colella P., Woodward P. R., 1984, J. Comput. Phys., 54, 174

Connerney J. E. P., Acuna M. H., Ness N. F., 1981, J. Geophys. Res., 86, 8370

Cranmer S. R., 1996, PhD thesis, Univ. Delaware

Czesla S., Schmitt J. H. H. M., 2007, A&A, 465, 493

Donati J.-F., Babel J., Harries T. J., Howarth I. D., Petit P., Semel M., 2002, MNRAS, 333, 55

Donati J.-F., Howarth I. D., Bouret J.-C., Petit P., Catala C., Landstreet J., 2006a, MNRAS, 365, L6

Donati J.-F. et al., 2006b, MNRAS, 370, 629

Drake S. A., 1998, Contrib. Astron. Observ. Skalnaté Pleso, 27, 382

Drake S. A., Linsky J. L., Schmitt J. H. M. M., Rosso C., 1994, ApJ, 420, 387

Ferrario L., Wickramasinghe D. T., 2005, MNRAS, 356, 615

Ferrario L., Wickramasinghe D. T., 2006, MNRAS, 367, 1323

Gagné M., Oksala M. E., Cohen D. H., Tonnesen S. K., ud-Doula A., Owocki S. P., Townsend R. H. D., MacFarlane J. J., 2005, ApJ, 628, 986

Gayley K. G., 1995, ApJ, 454, 410

Groote D., Hunger K., 1982, A&A, 116, 64

Hesser J. E., Ugarte P. P., Moreno H., 1977, ApJ, 216, L31

Hinton J. A., 2004, New Astron. Rev., 48, 331

Holder J., 2006, preprint (astro-ph/0611598)

Hubrig S., Briquet M., Schöller M., De Cat P., Mathys G., Neiner C., 2007, in Okazaki A. T., Owocki S. P., Štefl S., eds, ASP Conf. Ser. Vol. 361, Active OB-Stars: Laboratories for Stellar and Circumstellar Physics. Astron. Soc. Pac., San Francisco, p. 434

Krtička J., Kubát J., Groote D., 2006, A&A, 460, 145

Lacey C. G., 1988, ApJ, 326, 769

Landstreet J. D., Borra E. F., 1978, ApJ, 224, L5

Levinson A., Eichler D., 1992, ApJ, 387, 212

MacDonald J., Bailey M. E., 1981, MNRAS, 197, 995

Michel F. C., Sturrock P. A., 1974, Planet. Space Sci., 22, 1501

Mullan D. J., MacDonald J., 2005, MNRAS, 356, 1139

Nakajima R., 1985, Ap&SS, 116, 285

Owocki S., 2004, in Heydari-Malayeri M., Stee P., Zahn J.-P., eds, EAS Publ. Ser. 13, Evolution of Massive Stars, Mass Loss and Winds. EDP Sciences, France, p. 163

Owocki S. P., ud-Doula A., 2004, ApJ, 600, 1004

Pistinner S. L., Eichler D., 1998, MNRAS, 301, 49

Press W. H., Teukolsky S. A., Vetterling W. T., Flannery B. P., 1992, Numerical Recipes in Fortran, 2nd edn. Cambridge Univ. Press, Cambridge

Reale F., 1995, Comput. Phys. Commun., 86, 13

Riley P., Linker J. A., Mikić Z., Lionello R., Ledvina S. A., Luhmann J. G., 2006, ApJ, 653, 1510

Sanz-Forcada J., Franciosini E., Pallavicini R., 2004, A&A, 421, 715

Shore S. N., Brown D. N., 1990, ApJ, 365, 665

Skinner S., Cohen D., Gagne M., Owocki S., Townsend R., 2004, BAAS, 36, 1520

Smith M. A., Groote D., 2001, A&A, 372, 208

Smith N., Owocki S. P., 2006, ApJ, 645, L45

Smith R. K., Brickhouse N. S., Liedahl D. A., Raymond J. C., 2001, ApJ, 556, L91

Sobolev V. V., 1960, Moving Envelopes of Stars. Harvard Univ. Press, Cambridge

Spitzer L., 1962, Physics of Fully Ionized Gases, 2nd edn. Interscience, New York

Stanev T., 2004, High Energy Cosmic Rays. Springer-Praxis

Townsend R. H. D., Owocki S. P., 2005, MNRAS, 357, 251 (TO05)

Townsend R. H. D., Owocki S. P., Groote D., 2005, ApJ, 630, L81

Trigilio C., Leto P., Umana G., Leone F., Buemi C. S., 2004, A&A, 418, 593

Tsyganenko N. A., 1989, Planet. Space Sci., 37, 5

Tsyganenko N. A., Peredo M., 1994, J. Geophys. Res., 99, 199

ud-Doula A., Owocki S. P., 2002, ApJ, 576, 413

ud-Doula A., Townsend R. H. D., Owocki S. P., 2006, ApJ, 640, L191

von Zeipel H., 1924, MNRAS, 84, 665

White R. L., Chen W., 1995, in van der Hucht K. A., Williams P. M., eds, IAU Symp. 163, Wolf–Rayet Stars: Binaries, Colliding Winds, Evolution. Kluwer, Dordrecht, p. 438

APPENDIX A: THE MAGNETOHYDROSTATIC LIMIT

The RRM model is based on the magnetohydrostatic limit, where all velocities and time derivatives in the Euler equations (1)–(3) vanish. In this limit, the momentum equation becomes

$$\frac{\mathrm{d}p}{\mathrm{d}s} = \rho \boldsymbol{g}_{\mathrm{eff}} \cdot \boldsymbol{e}_s \qquad (A1)$$

(the $\boldsymbol{g}_{\mathrm{rad}}$ term is not present because the radiative acceleration scales with the velocity gradient; see Section 2.5). With the effective gravity expressed in terms of a scalar effective potential (cf. equation 16), we recover an equation describing magnetohydrostatic equilibrium along the field line:

$$\frac{\mathrm{d}p}{\mathrm{d}s} = -\rho \frac{\mathrm{d}\Phi_{\mathrm{eff}}}{\mathrm{d}s}. \qquad (A2)$$

Assuming that the stationary plasma has cooled to the stellar surface temperature T_*, the equation of state (34) is used to derive the density distribution

$$\rho = C \, \mathrm{e}^{-\Phi_{\mathrm{eff}}/a_*^2}, \qquad (A3)$$

where C is a constant of integration, and a_* is the isothermal sound speed introduced in Section 3.1.

In the vicinity of a local minimum (as sampled along a field line), the effective potential can be approximated by the second-order Taylor expansion:

$$\Phi_{\mathrm{eff}}(s) \approx \Phi_0 + \frac{(s - s_0)^2}{2} \Phi_0'', \qquad (A4)$$

where s_0 is the arc distance coordinate of the minimum. Here, primes are used to denote differentiation with respect to s, while a subscript 0 indicates evaluation at the minimum $s = s_0$. (The Φ_0' term in the expansion is by definition zero.) Substituting this expression into equation (A3) reveals a Gaussian density distribution,

$$\rho = \rho_0 \, \mathrm{e}^{-(s - s_0)^2/h_0^2}, \qquad (A5)$$

with ρ_0 a constant based on C, and

$$h_0 \equiv \sqrt{\frac{2a_*^2}{\Phi_0''}}, \qquad (A6)$$

the characteristic scaleheight.

In the case of a dipole field aligned with the rotation axis (i.e. $\beta = 0$), the effective potential minima are situated at the field-line summits, and thus $s_0 = 0$. It can then be shown that

$$\Phi_0'' \approx \frac{3GM_*}{r_{\mathrm{K}}^3} \qquad (A7)$$

in the limit $L \gg r_{\mathrm{K}}/R_{\mathrm{p}}$ (see TO05, their equation 18), where

$$r_{\mathrm{K}} = \left(\frac{GM_*}{\Omega^2} \right)^{1/3} = \frac{3R_{\mathrm{p}}}{2w^{2/3}} \qquad (A8)$$

is the Kepler corotation radius where the rotation velocity coincides with the orbital velocity. In the same limit, the disc scaleheight is approximated by

$$h_0 \approx h_\infty \equiv \frac{3a_*}{2w} \sqrt{\frac{R_{\mathrm{p}}^3}{GM_*}}, \qquad (A9)$$

which depends only on the rotation rate and the stellar parameters.

APPENDIX B: THE RADIAL VELOCITY DERIVATIVE

To evaluate the radial velocity derivative in equation (29), we first expand it as

$$\left(\frac{\partial v}{\partial \tilde{r}}\right)_{\tilde{\theta}} = \left(\frac{\partial v}{\partial s}\right)_L \left(\frac{\partial s}{\partial \tilde{r}}\right)_{\tilde{\theta}} + \left(\frac{\partial v}{\partial L}\right)_s \left(\frac{\partial L}{\partial \tilde{r}}\right)_{\tilde{\theta}}. \tag{B1}$$

The right-hand side of this expression includes the velocity gradients both along and across the field. To eliminate the cross-field gradient $(\partial v/\partial L)_s$, we similarly expand the polar velocity derivative as

$$\left(\frac{\partial v}{\partial \tilde{\theta}}\right)_{\tilde{r}} = \left(\frac{\partial v}{\partial s}\right)_L \left(\frac{\partial s}{\partial \tilde{\theta}}\right)_{\tilde{r}} + \left(\frac{\partial v}{\partial L}\right)_s \left(\frac{\partial L}{\partial \tilde{\theta}}\right)_{\tilde{r}}. \tag{B2}$$

Combining these two expressions, and after some straightforward algebra, we obtain

$$\left(\frac{\partial v}{\partial \tilde{r}}\right)_{\tilde{\theta}} = \left(\frac{\partial v}{\partial s}\right)_L \left(\frac{\partial s}{\partial \tilde{r}}\right)_L - \left(\frac{\partial v}{\partial \tilde{\theta}}\right)_{\tilde{r}} \left(\frac{\partial \tilde{\theta}}{\partial \tilde{r}}\right)_L. \tag{B3}$$

This equation is exact; however, under the assumption (30) that the polar velocity derivative can be neglected, the second term on the right-hand side vanishes, so that

$$\left(\frac{\partial v}{\partial \tilde{r}}\right)_{\tilde{\theta}} = \left(\frac{\partial v}{\partial s}\right)_L \left(\frac{\partial s}{\partial \tilde{r}}\right)_L = \left(\frac{\partial v}{\partial s}\right)_L \sec \chi. \tag{B4}$$

Here, the second equality follows from equations (6) and (7) and gives the final form (31) for the radial velocity derivative.

APPENDIX C: LINEAR PERTURBATION ANALYSIS

To investigate small-amplitude departures from the magnetohydrostatic equilibrium discussed in Appendix A, we employ a linear analysis. Equations (1) and (2) are subjected to small-amplitude disturbances; discarding terms of quadratic or higher order in the perturbation amplitude leads to the system of equations:

$$\frac{\partial \rho_p}{\partial t} + \frac{1}{A}\frac{\partial}{\partial s}(A\rho v_p) = 0, \tag{C1}$$

$$\frac{\partial \rho v_p}{\partial t} + \frac{\partial p_p}{\partial s} = -\rho_p \frac{d\Phi_{eff}}{ds}. \tag{C2}$$

Here, the subscript p denotes Eulerian (fixed-position) perturbations, while quantities without subscripts refer to the equilibrium

state. As before, the g_{rad} term has been dropped, and the g_{eff} term is expressed in terms of the effective potential Φ_{eff}; no term containing the unperturbed velocity v appears, because the equilibrium state is taken to be at rest.

To solve these equations, we make the approximations that (i) all perturbations share a time dependence of the form $e^{i\omega t}$; (ii) the Taylor expansion (A4) may be used to model the spatial variation of Φ_{eff}; (iii) the derivative dA/ds can be neglected and (iv) the perturbations are isothermal, with the temperature remaining at T_*. With these approximations, the governing equations for the spatial dependence of ρ_p in the vicinity of a potential minimum $s = s_0$ can be reduced to the single second-order equation:

$$h_0^2 \rho_p'' + 2(s - s_0)\rho_p' + \left(\frac{\omega^2 h_0^2}{a_*^2} + 2\right)\rho_p = 0. \tag{C3}$$

As before, primes denote differentiation with respect to s, and h_0 was defined in equation (A6). Subject to the boundary conditions that $\rho_p \to 0$ for $(s - s_0) \to \pm\infty$, the eigensolutions are readily found as

$$\rho_p(s) = a_m\, e^{-(s-s_0)^2/h_0^2}\, H_m[(s - s_0)/h_0], \tag{C4}$$

where a_m is a constant setting the amplitude of the perturbations, and H_m is the Hermite polynomial of integer degree $m \geqslant 0$. These normal modes have eigenfrequencies set by the characteristic equation

$$\omega = \omega_m \equiv \sqrt{2m}\frac{a_*}{h_0}. \tag{C5}$$

The fundamental ($m = 0$) mode has a zero frequency, and corresponds not to an oscillation, but to the addition of more mass to the disc. Higher order modes all conserve disc surface density [i.e. $(\sigma_d)_p = 0$], because

$$\int_{-\infty}^{\infty} e^{-x^2} H_m(x)\, dx = \int_{\infty}^{\infty} e^{-x^2} H_m(x) H_0(x)\, dx = 0 \tag{C6}$$

for $m = 1, 2, 3, \ldots$; the first equality is because $H_0(x) = 1$, while the second follows from the orthogonality of the Hermite polynomials with respect to the weighting function e^{-x^2} (see Abramowitz & Stegun 1972).

This paper has been typeset from a TeX/LaTeX file prepared by the author.